

Skoltech

Skolkovo Institute of Science and Technology

Skolkovo Institute of Science and Technology

**Dynamic polariton
condensation in organic
microcavities**

Doctoral Thesis

by

ANTON BARANIKOV

DOCTORAL PROGRAM IN PHYSICS

Supervisor

Professor Pavlos Lagoudakis

Co-Supervisor

Dr. Anton Zasedatelev

Moscow-2019

© Anton Baranikov

Abstract

The light-matter interaction brings a rich playground both for fundamental research and novel optical devices. Semiconductor microcavities is one of the smart ways to couple light and matter. The system is called strongly-coupled if the cavity photon and the semiconductor material exciton interact much faster than decay. Thanks to the coupling, new eigenstates are formed, known as exciton-polaritons. These quasiparticles are attracting widespread interest due to their unique properties arising from the hybrid light-matter nature. Intensive investigations led to experimental demonstrations of such intriguing phenomena as Bose-Einstein condensation and superfluidity. Aside from this fundamental research, polaritonics is actively investigated to build a platform for optical devices. In this regard, organic semiconductors are considered to be a promising material due to room-temperature operation, high oscillator strength, and ease of fabrication. The goal of this thesis is to get more insight into the physics of organic strongly-coupled microcavities to pave a way towards organic polariton devices.

List of Publications

1. Zasedatelev, Anton V., **Anton V. Baranikov**, Darius Urbonas, Fabio Scafrimuto, Ullrich Scherf, Thilo Stöferle, Rainer F. Mahrt, and Pavlos G. Lagoudakis. "A room-temperature organic polariton transistor." *Nature Photonics* (2019): 1., <https://doi.org/10.1038/s41566-019-0392-8>, **published**

Contribution: full, except sample fabrication

2. Kuzmina, Elena A., Tatiana V. Dubinina, Anton V. Zasedatelev, **Anton V. Baranikov**, Maria I. Makedonskaya, Tolganay B. Egorova, and Larisa G. Tomilova. "Hexadecachloro-substituted lanthanide (III) phthalocyaninates and their hybrid conjugates with gold nanoparticles: Synthesis and optical properties." *Polyhedron* 135 (2017): 41-48., **published**

Contribution: Z-scan investigation on nonlinear optical properties

3. Yagafarov, Timur, Denis Sannikov, Anton Zasedatelev, Kyriacos Georgiou, **Anton Baranikov**, Oleksandr Kyriienko, Ivan Shelyk et al. "On the origin of blueshifts in organic polariton condensates." *arXiv preprint arXiv:1905.02573* (2019)., **under review in Physical Review Letters**

Contribution: Examination of nonlinear refractive index change influence on the polariton blueshift

Acknowledgements

I would like to thank all the people to whom I am grateful and who has its own big or small contribution to my daily life during this adventure:

My supervisor, **Pavlos Lagoudakis**, who gave me the possibility to work in an amazing scientific atmosphere and guided me through the whole Ph.D. I will never forget the "school of life", that I passed here.

My co-supervisor, **Anton Zasedatelev**, who taught me a lot of things in the lab, with whom we worked sleepless nights and had a lot of extremely stimulating discussions. His support and guidance opened up new horizons and ways of thinking for me, which made this thesis possible. Also, it was my pleasure not only to work together, but also to have a lot of friendly talks.

My coffee-mate, **Sergey Alyatkin**, for various scientific and non-scientific discussions.

My lab-mates, especially **Kirill Sitnik, Stepan Baryshev, Denis Sannikov, Dmitriy Mikulik, Mael Brossard, Anton Putintsev, Alexander Averchenko, Timur Ermatov, and Alexis Askitopolos.**

My friend, **Timur Yagafarov**, for passing through the long (more than Ph.D) path together :)

And obviously, I would like to express my senior gratitude to my family: **my parents and my wife, Kamilla**, for the infinite support and endless trust.

Contents

Abstract	1
List of Publications	2
Acknowledgements	4
List of Abbreviations	7
List of Figures	9
List of Tables	17
1 Introduction	18
2 Polaritons background	22
2.1 Strong coupling and polaritons	22
2.1.1 Optical microcavity	22
2.1.2 Intracavity medium	26
2.1.3 Polaritons model	30
2.2 Polariton condensation	34
2.2.1 Inorganic polariton condensation	36
2.2.2 Organic polariton condensation	40
2.2.3 Inorganic vs. organic	44

3	Vibron-mediated polariton condensation	46
3.1	Introduction	46
3.2	Sample	47
3.3	Experiment	53
3.4	Results and discussion	56
3.5	Intracavity nonlinear refractive index influence	61
4	Polariton amplification	67
4.1	Introduction	67
4.2	Experiment	68
4.3	Organic polariton amplifier	70
5	All-optical polariton logic	78
5.1	Introduction	78
5.2	Organic polariton switching	79
5.3	OR and AND polariton logic gates	81
6	Conclusions and future research	85
	Bibliography	87

List of Abbreviations

- MBE - Molecular Beam Epitaxy
- LED - Light Emitting Diode
- OLED - Organic Light Emitting Diode
- BEC - Bose-Einstein Condensation
- DBR - Distributed Bragg Reflector
- IC - Internal Conversion
- LPB - Lower Polariton Branch
- MPB - Middle Polariton Branch
- UPB - Upper Polariton Branch
- FWHM - Full Width of Half Maximum
- ND - Neutral Density
- NA - Numerical Aperture
- EMCCD - Electron Multiplying Charge-Coupled Device
- PD - PhotoDetector
- LP - Low Pass edge filter
- SP - Short Pass edge filter
- OPA - Optical Parametric Amplifier
- WLC - White Light Continuum
- HPT - Hybrid Photomultiplier Tube
- APD - Avalanche PhotoDiode

VCSOA - Vertical-Cavity Semiconductor Optical Amplifier

QD SOA - Quantum-Dot Semiconductor Optical Amplifier

EDWA - Erbium-Doped Waveguide Amplifier RWA - rotating wave approximation

List of Figures

2.1	The schematic of an optical microcavity. Light is confined between the mirrors M1 and M2 having the separation distance of $\frac{\lambda_c}{2n_c}$	23
2.2	Optical microcavity with DBRs. (a) The sketch of a typical microcavity structure containing DBRs. (b) The red line shows a calculated reflectivity spectrum for a single DBR with 32 pairs of high and low refractive index materials (2.82 and 2.52). The black line depicts a calculated reflectivity spectrum for 16 and 24 pairs for top and bottom mirrors with a 2λ spacer.	25
2.3	A typical Jablonski diagram depicting molecular energy states together with possible transitions.	28
2.4	Optical properties of organic semiconductors. (a) A typical energy diagram for S_0 - S_1 transitions (b) The corresponding absorption and emission spectra illustrating the Fermi's golden rule.	29
2.5	Analog of light-matter interaction: two mechanical oscillators (masses m_A , m_B , spring constants k_A , k_B) coupled by a spring κ	31
2.6	Illustration of the strong exciton-photon coupling for three values of detuning.	34

2.7	Polariton lasing buildup in inorganic microcavities. (a) A relaxation route towards the ground polariton state under non-resonant pumping. (b) A schematic of polariton-polariton scattering.	36
2.8	Polariton amplification in an inorganic microcavity. (a), (b) A sketch of the pump-probe experiment together with illustration of the polariton-polariton scattering induced by the probe pulse. (c) The result of the probe intensity enhancement when the pump beam is on.	39
2.9	Relaxation towards polariton states under non-resonant pumping in organic microcavities. (a) Photoluminescence of the uncoupled exciton reservoir pumps the polariton states. (b) The exciton reservoir relaxes towards polariton states through the vibron emission.	41
2.10	Illustration of experimental hallmarks of polariton condensation. (a) Characteristic change in the angle-resolved photoluminescence going from the linear (before the threshold, the left panel) to the nonlinear regime (after the threshold, the right panel). (b) The emission integrated near $k_{\parallel} = 0$ (black squares) and spectral linewidth (blue circles) versus pump fluence illustrates the transition from the linear to the nonlinear regime. The polariton mode blueshift is shown as the inset.	43
3.1	The microcavity schematic. The central region of the cavity contains MeLPPP polymer sandwiched between two SiO_2 spacers. $\text{SiO}_2/\text{Ta}_2\text{O}_5$ alternating layers act as DBRs on the top and bottom of the microcavity. The whole structure is produced on the fused silica substrate.	48

3.2	The optical properties of MeLPPP. (a) Absorption and emission spectra reveal the vibronic structure of energetic levels. (b) Schematic representation of the energy levels of MeLPPP. (c) Raman spectrum of MeLPPP polymer shows three vibronic resonances.	50
3.3	Strong coupling of the optical microcavity containing MeLPPP polymer. (a) Reflectivity measurement (gray diamonds for dip positions) extended with photoluminescence data (red circles) is fitted by the coupled oscillator model. Two exciton eigenstates result in three polariton modes: LPB (blue line), MPB (green line) and UPB (orange line). Bare cavity (red dashed line) and exciton modes (brown dashed line for $S_{1,0}$ and gray dashed line for $S_{1,1}$) are also presented in the figure. (b) The calculated fractions of each polariton mode wavefunction. The red line presents the cavity eigenstate, while brown and gray depict $S_{1,0}$ and $S_{1,1}$ the exciton eigenstates, respectively. . . .	52
3.4	Reflectivity map of the optical microcavity obtained by the ellipsometer. (a) The reflectivity map shows the presence of the three polariton branches. (b) Zoomed-in part of the map demonstrates clear anti-crossing between MPB and UPB. . . .	53
3.5	Setup for the experiment described in Chapter 2. The excitation beam can be accurately tuned. The detection part enables both energy-resolved real space and momentum space imaging.	55

3.6	Momentum-resolved spectroscopy. (a) The Fourier plane projection on the spectrometer slit (depicted as gray transparent rectangles) results in k-space imaging of polariton luminescence. The slit cut the image along y-axis (b) The result polariton dispersion obtained by dispersing the energy of the Fourier plane slice.	56
3.7	The organic microcavity energetic structure and relevant relaxation paths upon "quasi-resonant excitation". Injected hot exciton reservoir (the red area) has two competing relaxation ways: 1) fast (within 100 fs) relaxation towards $S_{1,0}$ level (the blue area); 2) one-step relaxation forming polariton population in the ground state accompanied with the vibron emission (200 meV).	57
3.8	Polariton condensation upon "quasi-resonant excitation". (a) Normalized output emission image of the LPB dispersion above the threshold. The white dashed line is a fit for LPB below the threshold. (b) Output emission integrated over $k_{\parallel} = 0 \pm 0.5 \mu\text{m}^{-1}$ versus excitation density. The gray shaded area indicates the threshold. (c) Spectral characteristics (peak position of the emission spectrum - right/blue axis and the full width of half maximum (FWHM) - left/red axis) versus excitation density.	58

3.9	Output emission intensity versus the ground polariton state energy with fixed pump photon energy. The top x-axis presents corresponding energy difference between the ground state and the excitation photon (2.72 eV). The top graph depicts the Raman spectrum of MelPPP. The peaks of the measured dependence perfectly correlate with the vibronic resonances V1 and V2, e.g. when $\hbar\omega_{exciton} = \hbar\omega_{vibron} + \hbar\omega_{polariton}$	59
3.10	Output emission intensity versus the excitation photon energy with fixed ground polariton state energy. The dependence is plotted together with the polariton branches (left panel). The optical pump injects hot exciton reservoir. An increase of the emission intensity is observed when the resonant condition $\hbar\omega_{exciton} = \hbar\omega_{vibron} + \hbar\omega_{polariton}$ is met.	60
3.11	Schematic of Z-scan setup.	64
3.12	Z-scan results for the pure polystyrene film. (a) Open-aperture data for low (violet circles) and high (blue diamonds) intensity. (b) Close-aperture data for low (violet circles) and high (blue diamonds) intensity. The solid line depicts fitting curves for both plots.	65
4.1	Simplified schematic of the pump-probe setup. The detection part enables both energy-resolved real space and momentum space imaging. A flip mirror allows switching between the spectrometer and HPT for the weakest signals detection. The broadband probe beam is produced by WLC generation in a sapphire plate excited by residual 800 nm pump coming out from OPERA. The probe beam hits the sample at normal incidence seeding the ground polariton state.	69

4.2	Seeding the ground polariton state. (a) The spectrum of the broadband probe before the sample. (b) Energy and momentum resolve emission image obtained with the seeding by the probe. The white dashed line is a fit for LPB below the threshold (c) The spectrum of the probe after the sample.	70
4.3	The stimulation impact. (a) The dispersion image in the presence of the probe beam only. The white dashed line is a fit for LPB below the threshold. (b) The dispersion image in the presence of the pump beam only. (c) The dispersion image produced by both beams simultaneously hitting the sample. Integrated intensity is much greater than the summation of the "pump-only" and "probe-only" images.	71
4.4	Polariton condensation driven by the probe seeding. (a) The emission integrated near $k_{\parallel} = 0$ (over $\pm 0.5 \mu\text{m}^{-1}$) versus pump excitation density. The gray shaded area indicates the threshold. The dashed horizontal line indicates the pure probe intensity. (b) Spectral characteristics (peak position of the emission spectrum - right/blue axis and the full width of half maximum (FWHM) - left/red axis) versus excitation density. The probe beam fluence is kept at $\sim 20 \text{ nJ cm}^{-2}$	72
4.5	Comparison of "pump-probe" polariton condensation with the "pump-only" condensation. (a) The output emission intensity as a function of pump excitation density for "pump-only" (blue points) and "pump-probe" (red points) cases. Dashed lines show fits for linear, nonlinear and saturation regimes. (b) The ratio between both cases calculated from the (a) plot.	73

4.6	Polariton amplifier. (a) Schematic of an amplifier driven by "pump-probe" polariton condensation. (b) Transmission spectrum of the probe beam with (blue line) and without the pump beam (black line). For easier comparison the non-amplified probe is multiplied by 200.	74
4.7	Amplification versus incident probe fluence. The amplification is presented as SA (left/black axis) and g_{net} (right/red axis) .	75
4.8	Bidirectional amplification. (a) The weak transmitted probe signal (blue line) is amplified when the pump beam is present (red line). The non-amplified signal is multiplied by 200 for easier comparison. (b) The reflected probe beam (blue line) is amplified with almost the same SA (red line).	76
4.9	Angular dependence of the signal amplification. The probe beam fluence is kept at $\sim 20 \text{ nJ cm}^{-2}$ while the pump power is fixed at $180 \mu\text{J cm}^{-2}$	76
5.1	Organic polariton switching. (a) The principle of operation. The output emission is regarded as "1" state in the presence of two beams, while the "pump-only" emission is "0" state. (b) Extinction ratio defined as the emission intensity ratio between "1" and "0" states. (c) Output emission intensity of "pump-control" emission versus time delay between the two beams. Ultrafast temporal response of the switching is observed ($\sim 500 \text{ fs}$ at FWHM).	80

5.2	<p>Cascadability. (a) Schematic of the double pump-probe setup. (b) First stage amplification in the point A (Address 1, produced by Pump 1 and Control 1) is redirected back to the sample in the point B. The signal in the absence of Pump 2 is undetectable. (c) Pump 2 induces the second stage amplification (Address 2).</p>	81
5.3	<p>All-optical logic gates operation. (a) Schematic of the experimental configuration. Two address states I and II are produced powered by the same pump (Pump 1). Then, they are simultaneously retro-reflected to the point III and amplified by the Pump 2. I, II and III are regarded as two inputs and an output of a logic gate, respectively. The truth tables for an OR and an AND gates are also presented. (b) Control power dependences of the output emission under two regimes of excitation: the saturation regime (red dots) and below the "pump-only" condensation threshold. (c) Normalized real space emission images for all inputs configuration of the truth table for OR gate. (d) Normalized real space emission images for all inputs configuration of the truth table for AND gate.</p>	84

List of Tables

2.1	Inorganic vs. organic semiconductors as an intracavity medium for strong-coupling	45
4.1	Amplification coefficients in various types of optical amplifiers. The brackets present values in reflection configuration	77

Chapter 1

Introduction

Photonics is definitely one of the best examples illustrating how science can push society well-being. Majority of fields in medicine and technology are strongly influenced by photonics applications. Material processing, laser medicine, optical communications, biotechnology, cutting edge devices in industry and science are only possible due to the tremendous development of photonics [1]. The first successful laser demonstration by Maiman [2] attracted a lot of scientific attention to photonics owing to unique properties of laser radiation (high intensity, the possibility to transfer energy over long distances, narrow spectral bandwidth, etc.). In parallel, semiconductor materials research expanded with a high pace started with transistor invention by W.H. Brattain, J. Bardeen and W.B. Shockley at the Bell Laboratories in 1948. Following the first demonstration of the semiconductor laser in 1962 [3], it was well understood that semiconductor materials are crucial for further photonics development since they showed essential photonic functions such as light emission, absorption, and amplification. Successful research on semiconductor optical properties together with the rapid progress of epitaxial growth techniques (MBE - molecular beam epitaxy) opened the

road towards practical devices. To date, various semiconductor light emitting diodes (LEDs), photovoltaic elements, photodetectors, lasers, and amplifiers were demonstrated and successfully commercialized [4].

Another material approach in photonics started in 1966 with the first dye laser discovered independently by P. P. Sorokin and F. P. Schäfer [5,6]. Researchers recognized the wavelength tuning capability of dye lasers by modifying the chemical structure of organic matter and, in the following years, a lot of dye lasers from ultraviolet to the near-infrared spectral range (300–1200 nm) were shown [7]. Since tunability is considered to be one of the most important properties in terms of photonics applications, organic materials generated considerable interest among scientists. The next breakthrough happened in 1987 with the first organic light emitting diode (OLED) demonstration by Tang et al. [8]. Further progress on materials purity, new organic emitters, and coating techniques made OLEDs competitive with inorganic LEDs [7]. Aside from the wide-color range tunability, organic materials possess high quantum efficiency and low-cost fabrication, which makes them an inherent part of photonics development.

While photonics succeeded in straightforward devices like LEDs, lasers, and amplifiers, a new horizon for applications has been opened. All-optical logic received much attention in the past three decades since it is seen to be a prominent candidate to replace conventional electronics due to lower energy losses and higher information processing speed [9]. The first successful work on the all-optical switch (i.e. a device allowing to control light beam states "1" and "0" by another light beam) was done utilizing optical bistability effect [10]. Subsequent approaches exploit single molecules, quantum dots and atomic systems [11–13]. However, most of them failed to satisfy the necessary criteria for realization of large logic systems. All-optical logic is currently

seen as a promising area attracting widespread interest from physicists with various background.

Polaritonics recently demonstrated itself as a suitable platform for all-optical logic architecture [14–16]. Polaritons are quasiparticles originating from the strong interaction between light confined in a microcavity and matter embedded inside. In their groundbreaking paper [17], Weisbuch et. al. showed the first experimental evidence of strong light-matter interaction between inorganic semiconductor quantum wells and planar cavity. By measuring reflectivity spectra, they observed normal-mode splitting when the quantum wells and the cavity are in resonance. Subsequently, strongly-coupled microcavity structure was proposed as a coherent emission source [18]. Thanks to bosonic nature of polaritons, they are expected to undergo Bose-Einstein condensation (BEC) phenomenon resulting in coherent emission or lasing from the ground polariton state, firstly demonstrated by Kasprzak et al. [19]. Having non-equilibrium situation due to finite polariton lifetime, polariton thermalization, essential to BEC, is usually hard to achieve. However, lasing from the ground polariton state without thermalization is still possible and usually referred to a polariton laser [20]. Aside from the laser, polaritonics succeeded in other optical devices such as an optical amplifier, optical transistor, and even all-optical logic [16,21]. Besides the few exceptions [22,23], the room-temperature operation is prohibited in inorganic semiconductors. Indeed, weak bounding energy of elementary excitations in inorganic materials (Wannier-Mott excitons) decreases the working temperature down to values where excitons don't dissociate due to thermal excitations. The most suitable platform for ambient conditions is organic semiconductors owing to high bounding energy of organic Frenkel excitons. Discussed above advantages of organic materials instigated the rapid progress in organic polaritonics. Re-

cently, there were many experimental achievements starting from the first strong-coupling observation [24]. To date, linear polariton emission [25–27] and polariton lasing [28–31] with various materials encompassing wide spectral range were shown. Unfortunately, the localized nature of Frenkel excitons prevents polariton-polariton interaction, the crucial ingredient for a lot of achievements in inorganic polaritonics. For this reason, optical polariton devices at room temperature are still remain elusive and is a central part of this thesis. Throughout this work, the author elucidates a receipt for polariton lasing at ambient conditions a strongly-coupled microcavity containing an organic polymer. Thorough experiments reveal the driving mechanism of relaxation under non-resonant excitation. Further, the ultra-fast pump-probe technique allows for polariton amplification and dynamics investigation. Finally, "proof-of-concept" work is done to demonstrate the cascability, switching principle, and two optical logic gates operation. All the experiments are done under pulsed excitation, bringing the name of this thesis.

The thesis structure is organized in the following manner:

- 1) Experimental realization of vibron-mediated polariton condensation at room temperature;
- 2) Experimental realization of polariton amplification driven by bosonic stimulation and vibron-mediated relaxation at room temperature;
- 3) Experimental demonstration of the switching concept, the cascable operation and the principles of AND and OR logic gates

Chapter 2

Polaritons background

2.1 Strong coupling and polaritons

One of the ways to enable light-matter interaction is to embed a semiconductor material into an optical microcavity. Under certain conditions, the interaction (or coupling) is called strong, and the system cannot be viewed as pure elementary excitations: the cavity photon and the medium exciton. Instead, a new quasiparticle, polariton, is introduced. This chapter presents the basics of polaritons and relevant literature review. The main take-aways will be used throughout the experimental part of this thesis.

2.1.1 Optical microcavity

An optical cavity is often used to create large electromagnetic field intensity, which is possible due to a particular structure. A conventional Fabry-Perot cavity is composed of two perfectly aligned highly reflecting mirrors with a certain separation distance L_c [32]. Intracavity field is represented by two counter-propagating waves which interfere and result in a standing wave if a resonant condition is satisfied:

$$L_c = \frac{m\lambda_c}{2n_c} \quad (2.1)$$

where m is an integer, n_c is the cavity refractive index and λ_c is the wavelength. Evidently, there can be a lot of standing waves with different m , and each of them is termed the mode of the resonator. Practically, light is able to be transmitted through the cavity only at modes frequencies. If L_c is reduced to just several wavelengths, it is possible to have only several modes. In this case, the resonator is called optical microcavity. In this work, only single mode microcavities are considered, i.e. $L_c = \frac{\lambda_c}{2n_c}$ (see Figure 2.1).

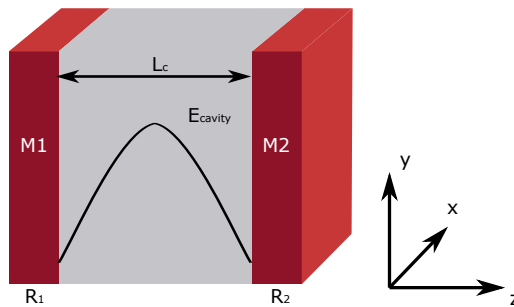


Figure 2.1: The schematic of an optical microcavity. Light is confined between the mirrors M1 and M2 having the separation distance of $\frac{\lambda_c}{2n_c}$.

Since mirrors have imperfect reflectivity, light leaks from the cavity. These losses are described quantitatively by a figure of merit, quality factor Q . It is determined by the ratio of electromagnetic energy U stored in the cavity at a given time to the rate of energy loss, normalized by the cavity frequency $\omega_c = \frac{2\pi c}{\lambda_c}$ [33]:

$$Q = \omega_c \frac{U}{dU/dt} \quad (2.2)$$

Solving the differential equation we obtain the following exponential dependence for the intracavity energy:

$$U(t) = U_0 \exp\left(\frac{-\omega_c t}{Q}\right) \quad (2.3)$$

where we can recall the characteristic lifetime of the mode $\tau = Q/\omega_c$. Corresponding electric field oscillations is written in the following form ($|E(t)|^2 \sim U(t)$):

$$E(t) = E_0 \exp\left(\frac{-\omega_c t}{2Q}\right) \exp(-i\omega_c t) \quad (2.4)$$

Standard Fourier transformation results in the frequency dependence:

$$U(\omega) \sim |E(\omega)|^2 \sim \frac{1}{(\omega - \omega_c)^2 + (\omega_c/2Q)^2} \quad (2.5)$$

It can be seen that the obtained transmission spectrum is represented by the Lorentzian shape with the full width of half maximum (FWHM) $\delta\omega = \omega_c/Q$. As long as the quality factor is dependent on the cavity losses, it is also can be determined by the mirrors reflection coefficients [32]:

$$Q \simeq \frac{\pi(R_1 R_2)^{1/4}}{1 - (R_1 R_2)^{1/2}} \quad (2.6)$$

One can think that metal is a perfect material for the mirrors. However, a typical semiconductor microcavity contains distributed Bragg reflectors (DBR) instead (see figure 2.2a). A DBR is a layered structure with alternating high and low refractive indexes. Each layer has $\lambda/4$ optical thickness. Consequently, light reflected from each interface interfere constructively providing perfect reflection from the structure in a spectrum region called stop-band. Applying transfer matrix method (TMM), it is calculated that the

maximum reflectivity is at the center of a stopband [33]. In fact, it can be more than 0.99 offering larger quality factors than metallic microcavities. The red line of figure 2.2b shows a typical reflectivity spectrum calculated by TMM [34], while the black line depicts the reflectivity for a microcavity with a 2λ spacer. As expected, a dip emerges for the latter case indicating the cavity mode.

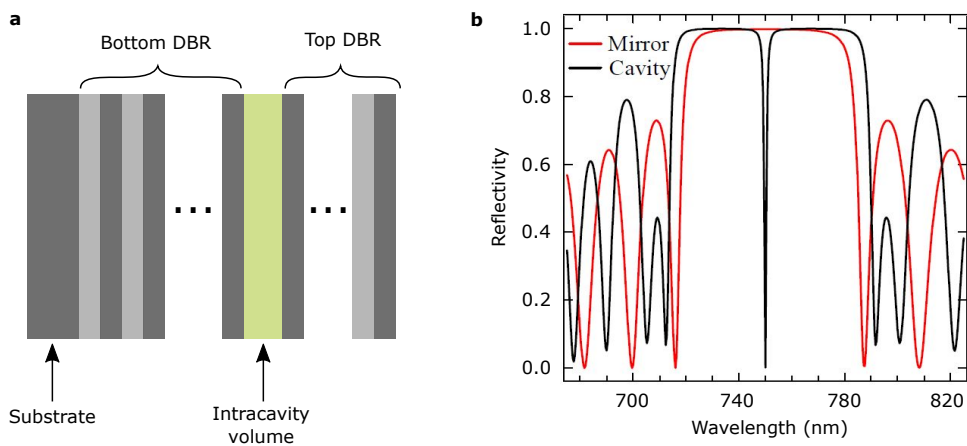


Figure 2.2: Optical microcavity with DBRs. (a) The sketch of a typical microcavity structure containing DBRs. (b) The red line shows a calculated reflectivity spectrum for a single DBR with 32 pairs of high and low refractive index materials (2.82 and 2.52). The black line depicts a calculated reflectivity spectrum for 16 and 24 pairs for top and bottom mirrors with a 2λ spacer. Adapted from [34].

A microcavity traps photons only in z-direction, not in xy plane. Consequently, it leads to the energy resonance dependence on the incident angle, i.e. angular dispersion. The energy of the confined photons depends on the total wavevector module k :

$$E_{cav} = \frac{\hbar c}{n_c} k = \frac{\hbar c}{n_c} \sqrt{k_{xy}^2 + k_z^2} \quad (2.7)$$

where k_{xy} is in-plane wavenumber depending on the angle of incidence, k_z is quantized, so that $k_z = \pi/L_c$. When $k_{xy} \ll k_z$, (2.7) can be transformed by Taylor expansion:

$$E_{cav} \simeq \frac{\hbar c k_z}{n_c} \left(1 + \frac{k_{xy}^2}{2k_z^2}\right) = E_{cav}(k_{xy} = 0) + \frac{\hbar^2 k_{xy}^2}{2m_{cav}} \quad (2.8)$$

Thus, the cavity dispersion has a parabolic form with the effective mass of the photons $m_{cav} = \pi n_c \hbar / c L_c$.

2.1.2 Intracavity medium

The next ingredient for the strong light-matter coupling is an absorbing material which is usually sandwiched between DBRs of an optical microcavity. This thesis is concentrated on organic semiconductors, usually implying any chemical compound containing carbon and possessing semiconducting properties. Organic molecules are formed by atoms bonded together by the overlap of electronic orbitals. Solid-state physics manifests that this connection results in an energy structure with a lot of levels, termed molecular orbitals. Electrons fill energy states up to the highest-energy occupied molecular orbital (HOMO), while levels above the lowest-energy unoccupied molecular orbital (LUMO) remain empty. As in the case of inorganic crystalline semiconductors, there is an energy gap composed of unavailable states, namely between the HOMO and LUMO. The HOMO and LUMO levels are analog for the top of the valence and the bottom of the conduction band of inorganic materials, respectively. We note that since there is organic and

inorganic polaritonics, drawing parallels between these types of materials is inevitable.

Under optical illumination of sufficient photon energy (more than a bandgap), an electron is excited from its ground state (LUMO) leaving a vacant place behind. This vacancy is represented by a positively charged quasiparticle, a hole. The mutual Coulomb attraction leads to the bound electron-hole pair called an exciton. Organic semiconductors typically possess Frenkel excitons with strong binding energy (0.5-1 eV) [35]. This case is completely different from inorganic materials (Wannier-Mott excitons) where high dielectric constant weakens the attraction. As a result, thermal energy at room temperature (~ 30 meV) can lead to the Wannier-Mott excitons dissociation into free electrons and holes, while the Frenkel excitons are robust at ambient conditions. An excited exciton tends to relax by giving its energy to the yet one particle, phonon or photon. These processes are called nonradiative or radiative recombination, respectively.

Molecular excited states are represented by a well-known Jablonski diagram (Figure 2.3) [36]. Within the Born-Oppenheimer (BO) approximation, the total energy of a molecule is comprised of two terms: $E_{total} = E_{electron} + E_{nuclei}$, where $E_{electron}$ is the energy of electrons with fixed nuclei coordinates and E_{nuclei} presents the nuclei motion. The latter is composed of vibrational and rotational energies so that $E_{total} = E_{electron} + E_{vib} + E_{rot}$ [37]. In further consideration, we omit rotational energies, which are usually small and contribute as a broadening of the levels [37]. In the figure 2.3 the electronic states are shown as S_0 , S_1 and S_2 . In turn, each of them is split into vibrational levels which can be visualized as the anharmonic oscillation of the nuclei bonded by springs.

After the absorption, an optically excited exciton undergoes the relaxation

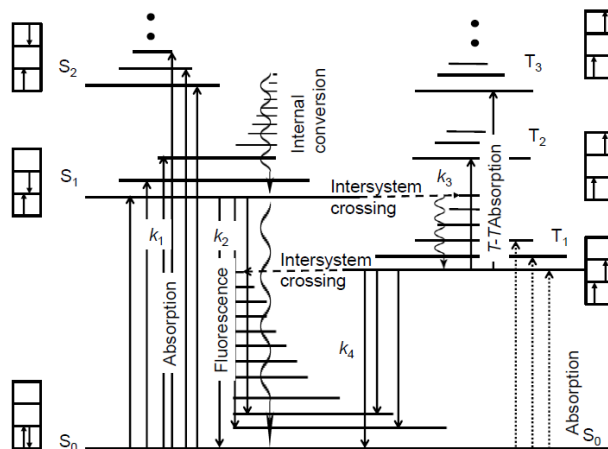


Figure 2.3: A typical Jablonski diagram depicting molecular energy states together with possible transitions [37].

towards the S_1 ground vibrational state by means of internal conversion (IC). IC is the process of giving the molecule energy to its surroundings and occurs on a short time scale ($\sim 10^{13} \text{ s}^{-1}$). The exciton can radiatively recombine accompanied with $S_1 \rightarrow S_0$ transition. Such a process is termed fluorescence. It most likely occurs from the ground vibrational excited electronic S_1 state because the fluorescence rate $k_2 \sim 10^6$ to 10^9 s^{-1} is much smaller than IC rate (Kasha's rule). The intersystem crossing also may be a source of the excited state decay. This process includes the electron spin flip and transition to so-called triplet levels T_1, T_2 and T_3 . However, the intersystem crossing has low probability in comparison with the other processes [37] and is not considered in this work.

To better understand the optical properties of organic semiconductors, the S_1 - S_0 transitions should be considered more carefully. The ground and first excited electronic states are split into vibrational levels induced by Morse potential presenting the anharmonic nuclei oscillations.

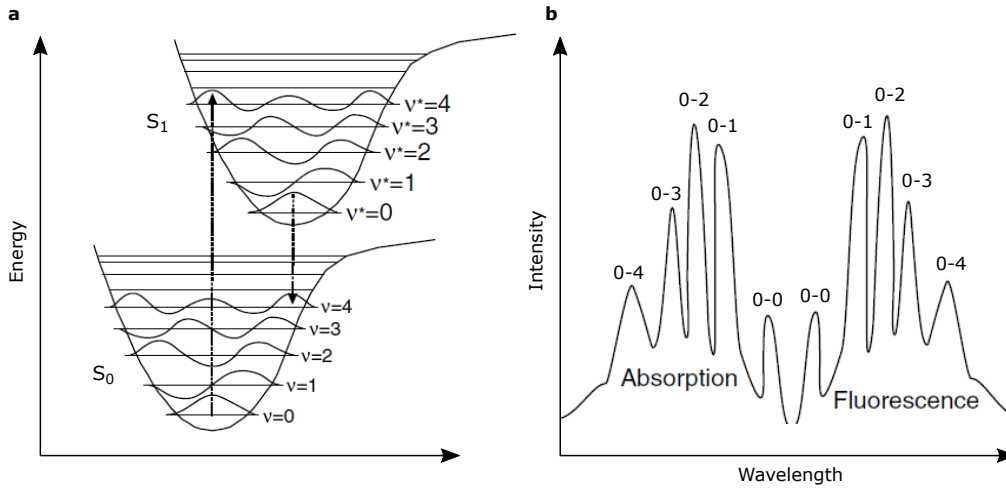


Figure 2.4: Optical properties of organic semiconductors. (a) A typical energy diagram for S_0 - S_1 transitions (b) The corresponding absorption and emission spectra illustrating the Fermi's golden rule. Adapted from [38].

Figure 2.4a shows an example of molecular energy levels versus the internuclear distance R for the simplest case of the diatomic molecule. Note that under optical excitation the nuclear separation is altered, resulting in the shifted potential for the S_1 level. We assume here, that the unexcited molecule starts with the ground electronic and ground vibrational state ($S_0, v = 0$) since normally the vibrational energy exceeds the room temperature thermal energy [38]. In this way, there are five possible transitions for both the absorption and the fluorescence: from $S_0, v = 0$ and $S_1, v^* = 0$ to all the vibrational levels ($v, v^* = 0, 1, 2, \dots$) of S_1 and S_0 , respectively. The probability of the transitions is defined by the Fermi's golden rule, which states that the transition rate is proportional to the wavefunctions overlap between the initial and final states [37]. Consequently, the spatial distributions of the wavefunctions and the nuclear displacement (Figure 2.4a) can interpret the typical absorption and fluorescence spectra being a mirror image of each

other with an energy shift (Figure 2.4b). This property is known as Frank-Condon principle [37]. Note that such spectra are usually obtained at low temperatures to exclude broadening effects. A careful reader may notice the spectral shift between 0-0 absorption and fluorescence peaks, which is not explained above. This feature is called the zero-phonon line Stokes shift and is typical for organic molecules. Usually, it can be produced by a lot of factors such as reabsorption, solvent effects, reorganization of the molecular structure in excited states, or inter/intramolecular energy transfer [36]. Since a particular organic semiconductor has a specific structure, every material should be considered separately. The Stokes shift for the polymer utilized in this thesis will be discussed in the experimental Section 3.2.

2.1.3 Polaritons model

To terminate the strong light-matter interaction receipt, an organic semiconductor should be utilized as an intracavity medium. If the microcavity mode is in resonance with the material optical transitions, the light-matter energy exchange is possible. Indeed, when the medium absorbs a photon, the excited exciton can radiatively recombine. The emitted photon is trapped in the cavity so that it has a chance to be absorbed by the medium one more time. Such periodic process can be viewed as energy exchange between two oscillators: the material exciton and the cavity photon. The most straightforward classical analog is two mechanical oscillators connected by a spring (Figure 2.5) [39].

Solving the differential equations of motion results in the eigenfrequencies of the system:

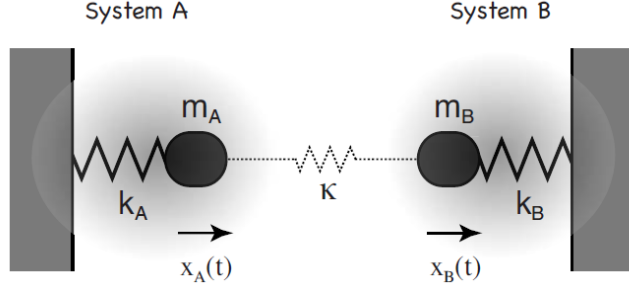


Figure 2.5: Analog of light-matter interaction: two mechanical oscillators (masses m_A , m_B , spring constants k_A , k_B) coupled by a spring κ . [39].

$$\omega_{\pm}^2 = \frac{1}{2}[\omega_A^2 + \omega_B^2 \pm \sqrt{(\omega_A^2 - \omega_B^2)^2 + 4\Gamma^2\omega_A\omega_B}] \quad (2.9)$$

where $\omega_A = \sqrt{(k_A + \kappa)/m_A}$, $\omega_B = \sqrt{(k_B + \kappa)/m_B}$ and $\Gamma = \frac{\sqrt{\kappa/m_A}\sqrt{\kappa/m_B}}{\sqrt{\omega_A\omega_B}}$. In the absence of the coupling and $m_A=m_B=m_0$, $k_A=k_B=k_0$, the solution corresponds to the uncoupled oscillations $\omega_0 = \sqrt{k_0/m_0}$. When the coupling is on, the frequency splitting emerges $\omega_+ - \omega_- = \Gamma$. Introducing the damping of the oscillators, it can be seen that the splitting is discerned only when $\frac{\Gamma}{\gamma_A/m_A + \gamma_B/m_B} > 1$, where γ_A and γ_B are the damping rates. In other words, the losses should be smaller than the coupling strength Γ . Such a regime is termed strongly coupled.

From the classical analog let us switch to the actual microcavity system. Here we introduce the quantum mechanical model of strongly coupled oscillators, which is the most powerful mathematical tool and widely used in the processing of experimental data [33]. The Hamiltonian of the uncoupled microcavity-matter system reads:

$$H_0 = \sum_{k_{\parallel}} E_{exc}(k_{\parallel}) b_{k_{\parallel}}^{\dagger} b_{k_{\parallel}} + \sum_{k_{\parallel}} E_{cav}(k_{\parallel}) a_{k_{\parallel}}^{\dagger} a_{k_{\parallel}} \quad (2.10)$$

where $(b_{k_{\parallel}}^{\dagger}, b_{k_{\parallel}})$ and $(a_{k_{\parallel}}^{\dagger}, a_{k_{\parallel}})$ are creation and annihilation bosonic operators for the exciton and the photon, respectively. The interaction Hamiltonian reads:

$$H_{int} = \sum_{k_{\parallel}} \hbar\Gamma (a_{k_{\parallel}}^{\dagger} b_{k_{\parallel}} + b_{k_{\parallel}}^{\dagger} a_{k_{\parallel}}) \quad (2.11)$$

The diagonalization of the total Hamiltonian leads to the eigenvalue problem:

$$\begin{pmatrix} E_{cav}(k_{\parallel}) & \hbar\Gamma \\ \hbar\Gamma & E_{exc}(k_{\parallel}) \end{pmatrix} \begin{pmatrix} \alpha \\ \beta \end{pmatrix} = E \begin{pmatrix} \alpha \\ \beta \end{pmatrix} \quad (2.12)$$

where (α, β) is the eigenvector and E are the eigenvalues. The solution gives the energy of new eigenstates of the system called upper and lower polaritons:

$$E_{UP,LP}(k_{\parallel}) = \frac{(E_{cav}(k_{\parallel}) + E_{exc}(k_{\parallel}))}{2} \pm \frac{\sqrt{(E_{cav}(k_{\parallel}) - E_{exc}(k_{\parallel}))^2 + 4(\hbar\Gamma)^2}}{2} \quad (2.13)$$

Thus, a new quasiparticle "polariton" is introduced. Evidently, it is a superposition of the exciton and photon. The coefficients $|\alpha|^2$ and $|\beta|^2$ have a physical meaning of photonic and excitonic contributions, known as Hopfield coefficients. Dependence on the in-plane wavevector k_{\parallel} gives the insight about the polariton dispersion. Figure 2.6 shows calculated polariton energies versus k_{\parallel} for three values of $|E_{cav}(k_{\parallel} = 0) - E_{exc}(k_{\parallel} = 0)|$ (known as exciton-photon detuning) [33]. While the cavity dispersion (Cav) has the parabolic shape (see Section 2.1.1), the exciton dispersion (Exc) is flat, i.e. the material absorption energy doesn't depend on the incident angle. Both curves are depicted as dashed lines. The calculated polariton dispersions are

shown as solid lines. The strong exciton-photon interaction results in the energy splitting between lower polariton and upper polariton branches (LPB and UPB), similar to the frequency splitting in the coupled mechanical oscillators. Note that the Eq. (2.13) differs from the Eq. (2.9). The reason for this mismatch is rotating wave approximation (RWA), within which the interaction Hamiltonian is derived (2.11) [33,40]. Under RWA, the Hamiltonian terms containing $|\omega_{cav} - \omega_{exc}| \ll \omega_{cav} + \omega_{exc}$ are dropped. The same approach reduces the solution for the classical oscillators to (2.13).

The energy difference between UPB and LPB at zero detuning (Figure 2.6b) is defined by $2\hbar\Gamma$. The splitting behavior is a classical signature of the strong interaction and usually probed experimentally either by angularly-resolved transmission or reflection spectroscopy. Both techniques are aimed to reveal the optical energy where the absorption of polariton states occurs.

In conclusion, both light and matter properties are important for the strong coupling realization. The interaction strength Γ (also known as Rabi frequency) characterizes the efficiency of the coupling and determined by light and matter parameters ($\Gamma \sim d$ and $\Gamma \sim 1/\sqrt{V_{cav}}$) [33,41], where d is the transition dipole moment of the material, i.e. probability of the absorption, V_{cav} is the intracavity volume. Hence, for the strong exciton-photon coupling, it is essential to have a highly absorptive material. Also, as was stated above, the exciton and photon damping rates should be small in comparison with Γ . These requirements significantly constrict the set of suitable organic materials, whereas optical microcavities should possess sufficient quality factor.

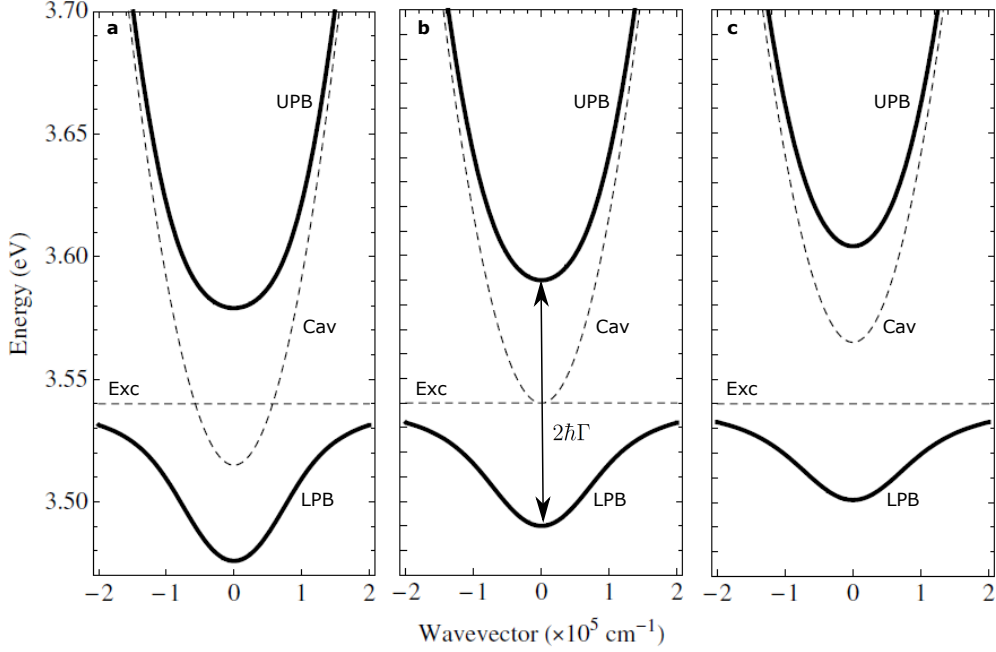


Figure 2.6: Illustration of the strong exciton-photon coupling for three values of detuning. Adapted from [33].

2.2 Polariton condensation

Polaritons have finite lifetime determined by the lifetimes of their counterparts: $\gamma_{LP} = |\alpha|^2\gamma_{photon} + |\beta|^2\gamma_{exciton}$, where γ is inversely proportional to the lifetime. Consequently, polaritons decay in the form of the emission from a microcavity, usually referred to as polariton photoluminescence [42]. The emitted photons carry the information about the internal polaritons such as energy, wavevector, states population. In this way, polariton properties can be studied experimentally. As was mentioned in Section 2.1.3., reflection or transmission spectroscopy is used as a proof for the strong coupling. During these experiments, an incident light resonantly populates polariton states. Hence, it undergoes losses, which are detected in the reflection or

transmission configuration. Conversely, the polariton photoluminescence is typically produced under non-resonant excitation. Created high energy excitons undergo relaxation towards polariton states populating upper and lower dispersions.

Since polaritons are a mixture of two bosons, they should exhibit bosonic properties [33]. One of them is an ability to massively occupy the same state which is prohibited for fermions due to Pauli exclusion principle. Also, polaritons obey final state stimulation stating that the rate of bosonic transition is proportional to the number of particles in the final state, more precisely to $(N_{final} + 1)$, where N_{final} is the final state population. These properties lead to polariton condensation, i.e. macroscopic population of the ground polariton state ($k_{\parallel} = 0$) by virtue of its minimal energy. This phenomenon is accompanied with a coherent laser-like emission under optical or electrical excitation. Thus, polariton condensation is also referred to as polariton lasing. Note that the term "condensation" doesn't imply Bose-Einstein condensation (BEC) [20] which is not considered in this work. Since polaritons are a system with losses, the polariton condensation is a threshold process. It is worth mentioning that the coherence of a polariton laser is reached by the process of stimulated relaxation of polaritons. It is completely different from a conventional laser, where the coherence occurs due to stimulated emission, requiring the population inversion. Thanks to that, the threshold of the polariton laser can be significantly lower [33].

Both, polariton photoluminescence and polariton lasing depend on the relaxation to polariton states following optical excitation. In the next subsections, we discuss the main driving mechanisms for inorganic and organic strongly-coupled microcavities.

2.2.1 Inorganic polariton condensation

The early demonstrations of polariton lasing were made in inorganic microcavities [43, 44], usually utilizing quantum wells produced from typical semiconductor materials: GaAs, CdTe, GaN, ZnO, etc. A standard route for the condensation buildup can be described in the following way (Figure 2.7a). After non-resonant optical excitation, a high energy hot excitons (the red area) relax down via interparticle scattering and optical phonons emission. Consequently, a large amount of excitons is formed at the exciton energy, termed a reservoir. Through acoustic phonons emission, the excitons scatter into polariton states which in turn dissipate their energy. Moving down across the LPB, polaritons become mostly photon-like, i.e. decreasing their lifetime. Consequently, the relaxation depends on the interplay between polariton leakage and polariton-phonons scattering rates. These two factors lead to the congestion of polaritons near the inflection point of the LPB (the black areas), called "bottleneck" [20].

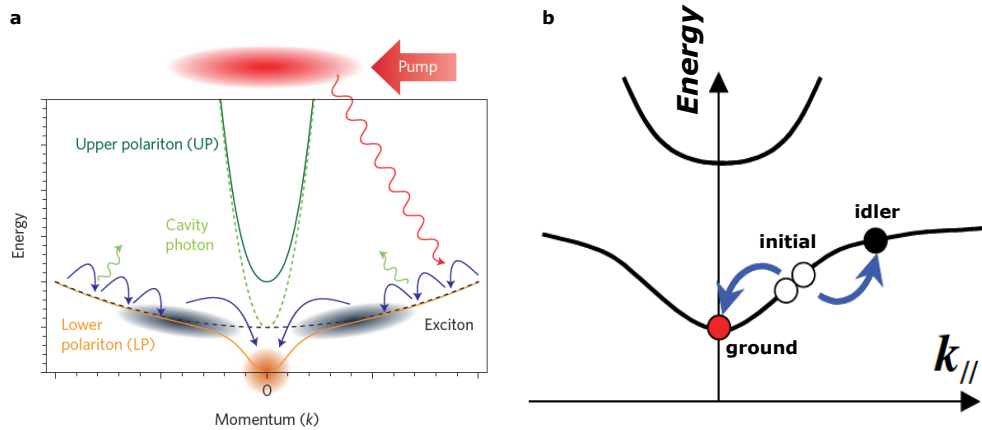


Figure 2.7: Polariton lasing buildup in inorganic microcavities. (a) A relaxation route towards the ground polariton state under nonresonant pumping. Taken from [20]. (b) A schematic of polariton-polariton scattering [42].

Indeed, the dispersion steepness increases at this point so that a larger amount of energy dissipation is needed for further relaxation towards the ground polariton state. Since the low energy acoustic phonons (~ 1 meV) can't handle this, polaritons leak out from the cavity in the form of photoluminescence. Strictly speaking, the relaxation strongly depends on the particular structure, since the dispersion shape, polariton lifetime, temperature, and phonons density of states affect the particles scatterings. For example, it was shown that for positive detunings, the bottleneck effect could be suppressed thanks to exciton-like LPB in this case [45]. In fact, the bottleneck can be overcome by another mechanism. Sufficient polariton density can provide efficient polariton-polariton scattering induced by the ground state stimulation. One can consider two polaritons scattering from the bottleneck region (Figure 2.7b): towards the ground state and the higher energy "idler" state ruled by the conservation laws:

$$2k_{initial} = 0 + k_{idler} \quad (2.14)$$

$$2E_{initial} = E_{ground} + E_{idler} \quad (2.15)$$

Hence, a macroscopic population in the ground state is formed after some pumping threshold [45–47]. Experimentally, it is observed as a superlinear increase of the emission from the $k_{\parallel} = 0$ polariton state.

Another way to obtain polariton condensation is resonant pumping. This technique relies on the polariton-polariton scattering mechanism similar to Figure 2.7b, pumping directly in the initial state. In this case, it is necessary to choose "the magic angle" where the conservation laws (2.14) and (2.15) are satisfied. Again, significant emission from the ground polariton state at some excitation threshold is observed [48]. Interestingly, such pumping regime brought the polariton amplification [21]. In this experiment, pulsed

excitation was used. Additionally, the probe pulse was introduced resonantly seeding the ground polariton state (see Figure 2.8a,b). Created preoccupation at $k_{\parallel} = 0$ triggered the scattering of polaritons produced by the pump pulse. Consequently, strong enhancement of the probe intensity was observed in the presence of two beams (Figure 2.8c) while there was almost no emission without the probe pulse. Subsequently, there were several demonstrations of the polariton amplification. In the best experiment, the microcavity exhibit the probe gain up to 5000 [49].

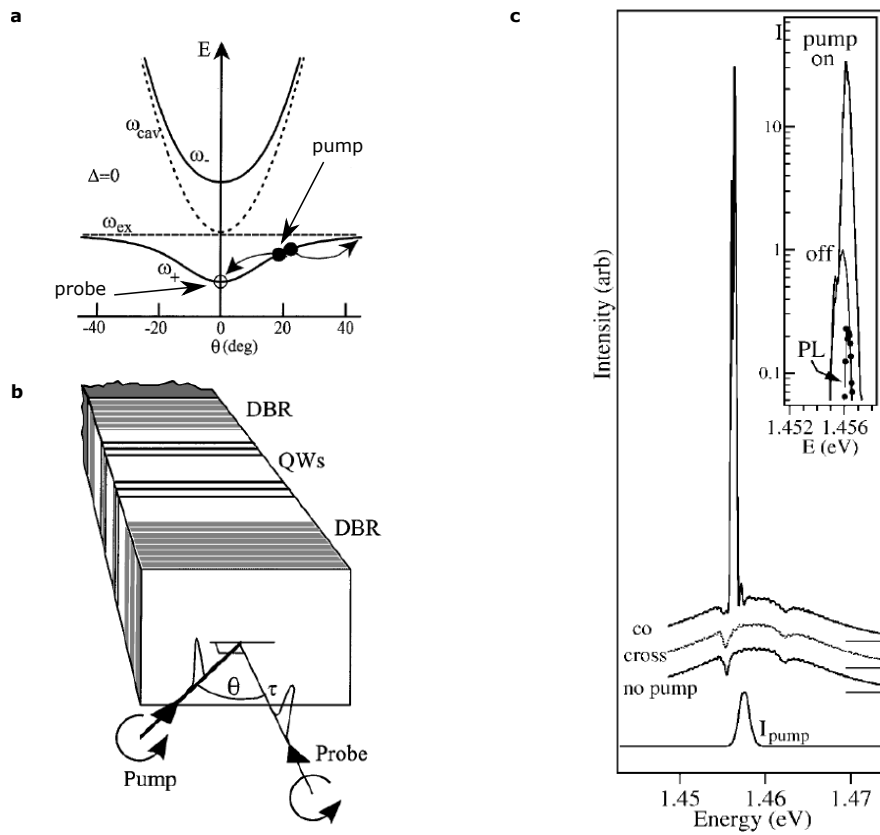


Figure 2.8: Polariton amplification in an inorganic microcavity. (a), (b) A sketch of the pump-probe experiment together with illustration of the polariton-polariton scattering induced by the probe pulse. (c) The result of the probe intensity enhancement in the reflection geometry when the pump beam is on. Adapted from [21].

2.2.2 Organic polariton condensation

Organic structures possess mechanisms of the condensate formation which are different from the inorganic ones. The low dielectric constant brings high bounding energy of Frenkel excitons and small spatial distribution. Thus, the localized nature weakens exciton-exciton Coulomb interactions [33]. Since polaritons interact with each other through their excitonic component, polariton-polariton interactions can't be a driving mechanism for the organic polariton lasing. So far, there was no experimental evidence of paired polariton scattering similar to [21].

The first polariton condensation in a crystalline organic strongly-coupled microcavity was demonstrated by Kena-Cohen et al. in 2010 [28]. Afterward, more demonstrations exploited a conjugated polymer, a fluorescent protein, and disordered dyes [29–31]. So far, theoretical works consider two main driving mechanisms of the relaxation towards polariton states [50–53]. Following the non-resonant optical excitation, fast relaxation forms the reservoir in the vicinity of the bare exciton energy. It should be noted that the uncoupled exciton reservoir coexists with polariton states [50, 52, 54]. Then, there are two ways of excitons relaxation towards polariton states. The first one is radiative pumping provided that photoluminescence spectrum of the organic material overlaps with the LPB. The second mechanism is non-radiative and utilizes the molecular vibrations. Here, if the energy difference between the exciton and the polariton state is resonant with the vibron ($E_{exc} - E_{polariton} = E_{vib}$), efficient relaxation of the exciton reservoir towards the polariton state occurs accompanied with the vibron emission. Hence, both mechanisms can lead to enough population to form the polariton lasing. Evidently, special engineering of the structure is needed. Figure 2.9 summarizes the above.

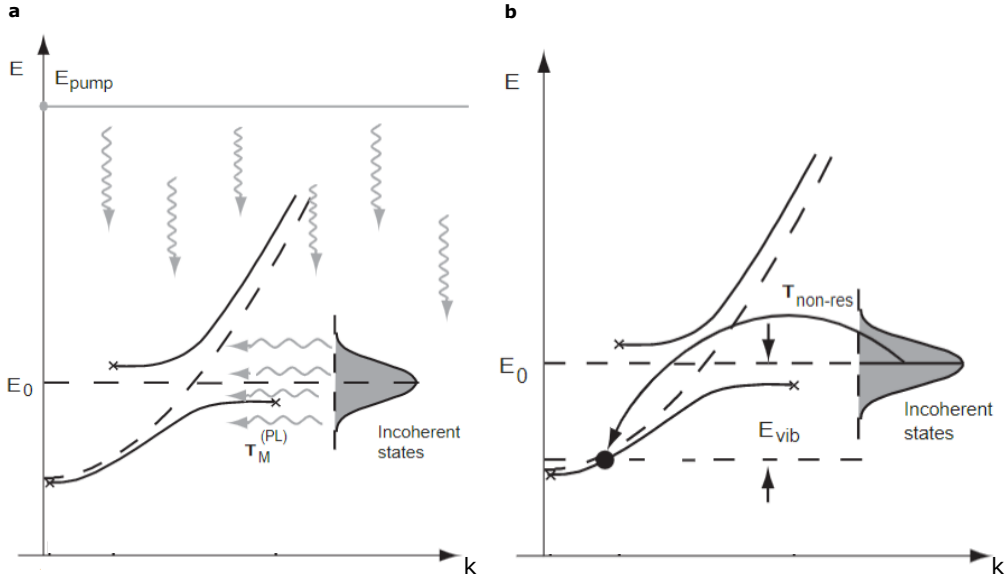


Figure 2.9: Relaxation towards polariton states under non-resonant pumping in organic microcavities. (a) Photoluminescence of the uncoupled exciton reservoir pumps the polariton states. (b) The exciton reservoir relaxes towards polariton states through the vibron emission. Adapted from [51].

Both inorganic and organic condensation has several hallmarks, crucial for the identification. Besides the superlinear increase of the polariton emission intensity at $k_{\parallel} = 0$, it is narrowing of the spectral linewidth (temporal coherence) and the energy blueshift. The latter is explained by Coulomb interactions between Wannier-Mott excitons in inorganic structures [55] and still is open to debate in organics [56]. Moreover, the system under the lasing should stay in the strong-coupling regime so that the blueshift can't exceed the difference between the ground polariton state and the bare cavity mode. Figure 2.10 presents the data from [57] illustrating all the mentioned points. Figure 2.10a shows the characteristic change in the angle-resolved photoluminescence going from the linear (before the threshold, the left panel) to the

nonlinear regime (after the threshold, the right panel). The emission integrated near $k_{\parallel} = 0$ (black squares) and spectral linewidth (blue circles) versus pump fluence are depicted in Figure 2.10b, the polariton mode blueshift is shown as the inset.

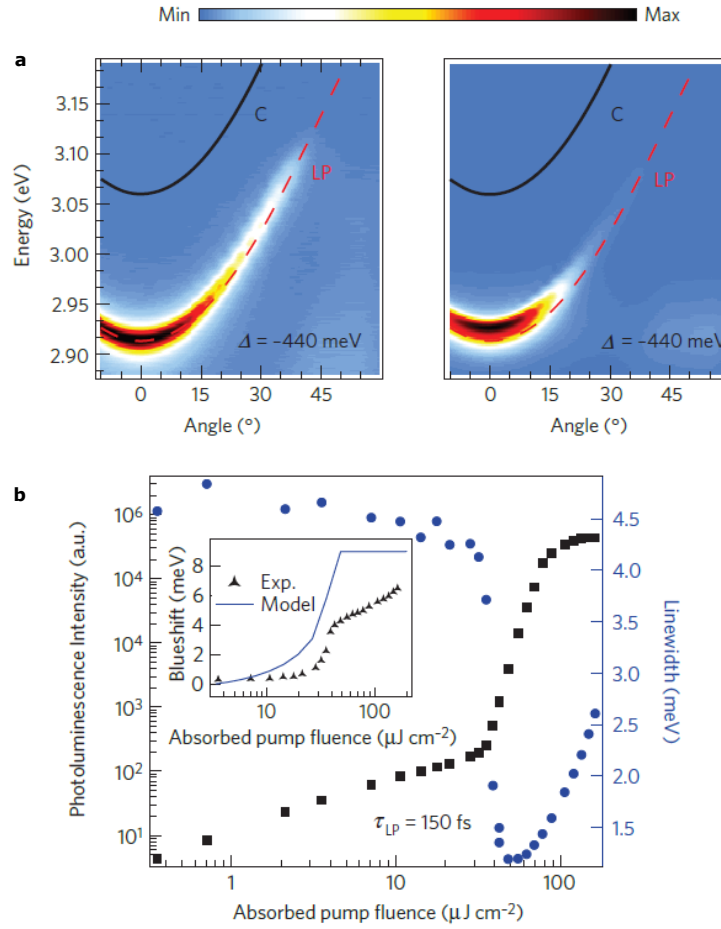


Figure 2.10: Illustration of experimental hallmarks of polariton condensation. (a) Characteristic change in the angle-resolved photoluminescence going from the linear (before the threshold, the left panel) to the nonlinear regime (after the threshold, the right panel). (b) The emission integrated near $k_{\parallel} = 0$ (black squares) and spectral linewidth (blue circles) versus pump fluence illustrates the transition from the linear to the nonlinear regime. The polariton mode blueshift is shown as the inset. Adapted from [57].

2.2.3 Inorganic vs. organic

Organic semiconductors have numerous advantages for strongly-coupled microcavities. The large binding energy of Frenkel excitons (0.5-1 eV) gives them the ability to survive at room temperature, while typical inorganic materials such as GaAs and CdTe possess weakly bound Wannier-Mott excitons (5-25 meV) [35]. Strictly speaking, such inorganic semiconductors as ZnO and GaN can persist at ambient conditions (binding energy \sim 25-60 meV). However, methods of growth of these materials are immature [58]. To date, there were a few demonstrations of polariton lasing in such structures [22,23]. Also, organics offer a much higher diversity of materials which led to numerous realizations of polariton lasing in the visible range from 2.1 to 3 eV [28–31,57].

As was discussed in Section 2.1.3, high absorption of the intracavity medium is crucial for the strong coupling. Frenkel excitons possess higher oscillator strength than Wannier-Mott resulting in larger Rabi splitting [35]. Consequently, organic microcavities are more tolerant to damping rates of the photon and exciton.

Unfortunately, organic microcavities have disadvantages. Exciton linewidth tends to be inhomogeneously broadened due to non-radiative losses and inhomogeneous structure of long polymers. Moreover, exciton energy depends on the molecular environment being different across the film and affected by fabrication procedures. Although organic materials are relatively easy to produce by solution processing and spin-coating, they are very sensitive to sputtering techniques used for DBRs deposition [58]. Consequently, the medium can be damaged, which leads to nonuniform deposition of the top DBR. It reduces the quality factor of the cavity and makes the polariton lifetime lower (tens to hundreds of fs) than in inorganic structures (few to tens

ps) [33]. It is also worth mentioning that the current low quality of organic microcavities samples causes the necessity of pulsed excitation with high fluence usually reaching tens to hundreds $\mu J/cm^2$, while the polariton lasing in inorganic structures can be obtained by continuous wave pumping. Table 2.1 summarizes the comparison between organic and inorganic materials.

Table 2.1: Inorganic vs. organic semiconductors as an intracavity medium for strong-coupling

	Inorganic	Organic
Exciton binding energy	Low (5-60 meV)	Large (0.5-2 eV)
Wide spectral range	-	+
Rabi splitting	Low (3-150 meV)	Large (0.1-1 eV)
Polariton lifetime	Large (few to ten ps)	Low (tens to hundreds fs)
Low excitation intensity	+	-
Persistent to DBR deposition	+	-

Summary: This chapter introduced the polariton basics by the consecutive description of optical microcavities, organic semiconductors and strong-light matter interaction. Then, we proceeded with polariton condensation phenomena and explained different relaxation mechanisms for inorganic and organic strongly-coupled microcavities. Finally, we made a comparison between these structures.

Chapter 3

Vibron-mediated polariton condensation

3.1 Introduction

As was discussed in Section 2.2.2, the important role of molecular vibrations in polariton states population was already explored theoretically both below and above the condensation threshold. Moreover, it was demonstrated experimentally below the threshold [59, 60]. In this chapter, we exploit vibron-mediated relaxation to achieve polariton condensation in an organic strongly-coupled microcavity. In contrast to usual non-resonant pumping, "quasi-resonant" excitation condition is realized. The term "quasi-resonant" is referred to special adjustment of the pump photon energy to be one vibronic molecular energy quantum (vibron) above the ground polariton state energy. Such configuration allows for efficient one-step exciton reservoir relaxation towards the ground polariton state accompanied with a vibron emission. We show the profound role of vibrons in polariton condensate population and sufficient reduction of the threshold in comparison with non-resonant exci-

tation. The structure of this chapter is organized as follows. Section 3.2 introduces the investigated organic microcavity, including optical properties of the intrinsic medium and coupled oscillator model. After that, Section 3.3 gives the experimental details on the excitation and detection schemes. Finally, Section 3.4 provides the data of the main results with discussions.

3.2 Sample

The optical microcavity consists of a bottom DBR, a central region containing 35 nm methyl-substituted ladder-type poly-[paraphenylene] (MeLPPP) layer sandwiched between two 50 nm SiO_2 spacers and a top DBR (see Figure 3.1). The bottom DBR consisting of 6.5 $\text{SiO}_2/\text{Ta}_2\text{O}_5$ quarter-wavelength-thick layers is deposited on a fused silica substrate via reactive ion sputtering. In contrast to the DBR, SiO_2 spacers are produced with a SiO_2 sputter target. Such a deposition process doesn't involve an oxygen plasma, which can destruct the organic material. With its rigid polymer backbone, the MeLPPP layer is sufficiently robust to withstand the spacers deposition without noticeable degradation. Subsequently, the SiO_2 spacer layer protects during the top DBR deposition (9.5 $\text{SiO}_2/\text{Ta}_2\text{O}_5$ layers) which again is done by reactive ion sputtering. In turn, the polymer layer is made by dissolving in the toluene and subsequent spin-coating on the bottom spacer layer. For the detailed process of MeLPPP synthesis see [61].

As already mentioned, the conjugated MeLPPP polymer has a rigid backbone provided by a methylene bridge between phenyl rings. Moreover, it has high intrachain order and short conjugation length distribution [62]. For these reasons, MeLPPP is expected to have sharp optical transitions and high quantum yield. To explore the main optical properties of MeLPPP,

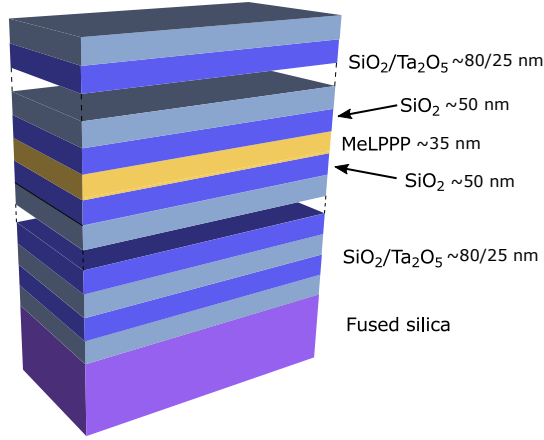


Figure 3.1: The microcavity schematic. The central region of the cavity contains MeLPPP polymer sandwiched between two SiO_2 spacers. $\text{SiO}_2/\text{Ta}_2\text{O}_5$ alternating layers act as DBRs on the top and bottom of the microcavity. The whole structure is produced on the fused silica substrate.

a spin-coated 100 nm-thick film is investigated. We measure the absorption spectrum of the polymer (Figure 3.2a - black) and identify two optical transitions at 2.72 eV (456 nm) and 2.91 eV (426 nm). In turn, the emission spectrum (Figure 3.2a - red) study results in a mirror image of the absorption spectrum with emission peaks at 2.68 eV (462 nm) and 2.51 eV (494 nm). These absorption/emission picture can be interpreted as electronic and vibronic transitions dictated by the Frank-Condon principle. Figure 3.2b shows the corresponding energetic diagram with $S_{0,0} \rightarrow S_{1,0}$ (0-0), $S_{0,0} \rightarrow S_{1,1}$ (0-1), $S_{1,0} \rightarrow S_{0,0}$ (0-0) and $S_{1,0} \rightarrow S_{0,1}$ (0-1) transitions. The Stokes shift of the zero phonon line can be produced by several reasons such as solvent effects, reorganization of the molecular structure in excited states, or inter/intramolecular energy transfer (see Section 2.1.2). However, these pure structural processes are often blurred by reabsorption of the highest-energy photons resulting in the redshift of the luminescence. The resulting Stokes

shift is observed to be ~ 0.06 eV in ladder-type polymers like MeLPPP [37]. To resolve pure effects, one can perform single-molecule spectroscopy measurements. In this way, it was shown that excited state reorganization causes only a small Stokes shift ~ 0.01 eV due to the rigid backbone of the MeLPPP polymer [63], while the intramolecular energy transfer affected much stronger (up to 0.04 eV). The latter effect manifests the energy migration towards parts of the molecules with larger wavelength emission resulting in the Stokes shift of the zero-phonon line. The observed Stokes shift (Figure 3.2a) is attributed to all of three reasons listed above. Since non-resonant excitation is frequently used for polariton systems, it is essential to understand the dynamics of high energy excited states. In MeLPPP vibrationally dressed $S_{1,1}$ state relaxes by means of internal conversion (IC) to the lowest excited state $S_{1,0}$ via vibrational relaxation within 100 fs [64]. In order to obtain the energy of vibronic quantum, we perform the non-resonant Raman spectroscopy (532 nm) of the polymer film, which is a powerful tool for understanding the composition of organic materials. Figure 3.2c depicts the resulting spectrum indicating three strongest vibronic resonances in the system: 1320 cm^{-1} (164 meV), 1568 cm^{-1} (194 meV) and 1604 cm^{-1} (199 meV). This result is consistent with other measurements in several works [65–67]. Following the interpretation of the spectrum from the literature, V1 resonance is attributed to interring CC stretching oscillations (i.e., along the line of the chemical bonds). V2 and V3 peaks present aromatic intra-ring CC stretching modes.

To verify strong-coupling between the exciton and photon modes, angular dependent reflectivity measurement (transverse-electric polarization) of the microcavity sample is performed. Broadband illumination produced by a stabilized tungsten-halogen light source is focused on the sample by an objective to $500\text{ }\mu\text{m}$ spot. An iris is placed before the objective restricting the solid

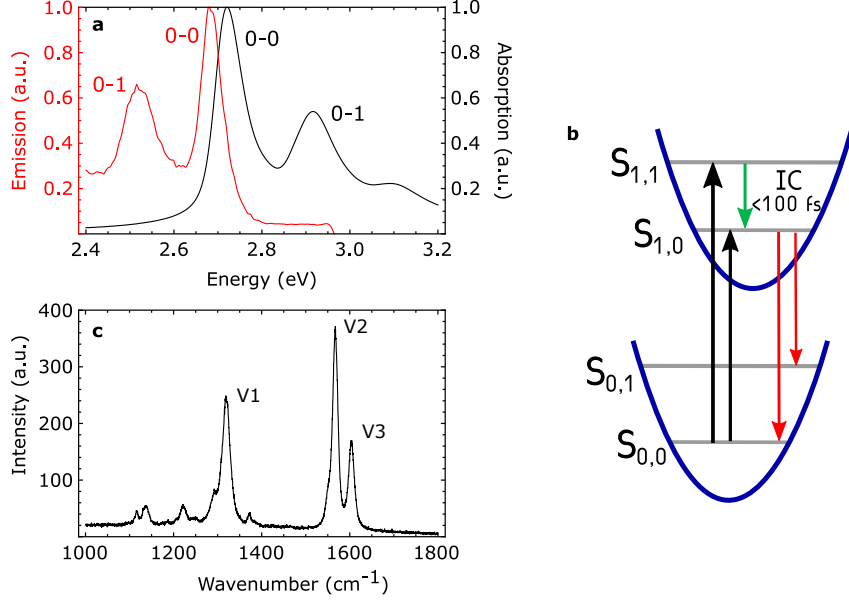


Figure 3.2: The optical properties of MeLPPP. (a) Absorption and emission spectra reveal the vibronic structure of energetic levels. (b) Schematic representation of the energy levels of MeLPPP. (c) Raman spectrum of MeLPPP polymer shows three vibronic resonances.

illumination angle to $\sim 5^\circ$. The obtained data is then fitted by the coupled oscillator model introduced in Chapter 2. Two exciton energy eigenstates $S_{1,1}$ and $S_{1,0}$ result in 3x3 total Hamiltonian of the system written in the following form:

$$\hat{H} = \begin{pmatrix} E_{cav}(\theta) & \hbar\Omega_1 & \hbar\Omega_2 \\ \hbar\Omega_1 & E_{exc,v=0} & 0 \\ \hbar\Omega_2 & 0 & E_{exc,v=1} \end{pmatrix}$$

where $E_{cav}(\theta) = E_{cav}(0)(1 - \sin^2(\theta)/n_{eff}^2)^{-1/2}$ is the cavity photon mode dispersion, $E_{exc,v=0}$ and $E_{exc,v=1}$ are exciton energy eigenstates, $\hbar\Omega_1$ and $\hbar\Omega_2$ are interaction strengths for $S_{0,0} \rightarrow S_{1,0}$ and $S_{0,0} \rightarrow S_{1,1}$ optical transitions,

respectively. The diagonalization of the Hamiltonian gives three polariton eigenstates: lower, middle and upper branches (LPB, MPB and UPB). Figure 3.3a shows the experimental data (gray diamonds indicate dip positions from measured reflectivity spectra) together with the applied fitting model. The interaction strengths and the cavity mode at $k_{\parallel} = 0$ are fit parameters while exciton energies (2.72 eV, 2.91 eV) and refractive index n_{eff} (1.75) are kept constant. The best agreement with the data is found when $\hbar\Omega_1=72$ meV, $\hbar\Omega_2=54$ meV and $E_{cav}(0)=2.65$ eV. Note that we add in the plot data obtained by photoluminescence measurement (red circles, see the details in Section 3.3) which is perfectly correlated with the reflectivity data. Figure 3.3b shows the polariton wavefunction composition calculated as the Hopfield coefficient for each of the three polariton branches. The result fractions of LPB are 72% of bare photon, 26% and 2% of $S_{1,0}$ and $S_{1,1}$ bare exciton, respectively.

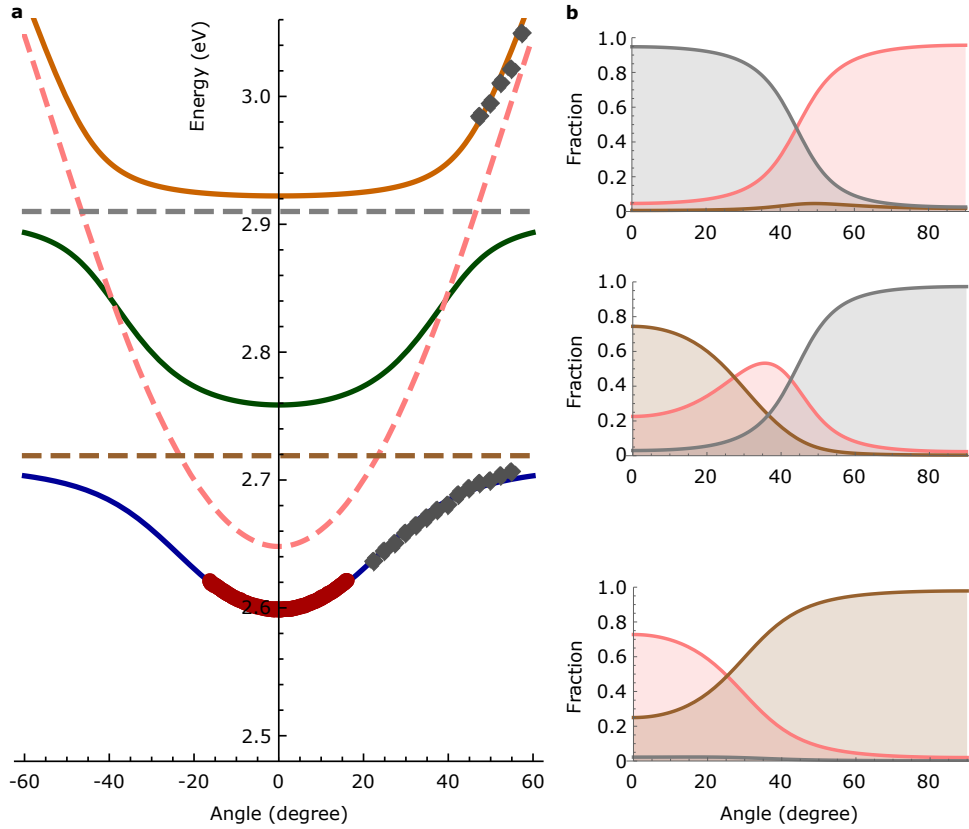


Figure 3.3: Strong coupling of the optical microcavity containing MeLPPP polymer. (a) Reflectivity measurement (gray diamonds for dip positions) extended with photoluminescence data (red circles) is fitted by the coupled oscillator model. Two exciton eigenstates result in three polariton modes: LPB (blue line), MPB (green line) and UPB (orange line). Bare cavity (red dashed line) and exciton modes (brown dashed line for $S_{1,0}$ and gray dashed line for $S_{1,1}$) are also presented in the figure. (b) The calculated fractions of each polariton mode wavefunction. The red line presents the cavity eigenstate, while brown and gray depict $S_{1,0}$ and $S_{1,1}$ the exciton eigenstates, respectively.

In addition, we extend the reflectivity data with more accurate measurements. Using high-sensitive ellipsometer (Woollam VASE), the reflectivity map is obtained (Figure 3.4a). The measurement is performed at a slightly different point on the sample. Nevertheless, the good agreement with the fitting model (black lines for the three polariton branches) is found. In contrast to the previous measurement, MPB is more pronounced as can be seen in Figure 3.4b depicting zoomed-in part of the reflectivity map.

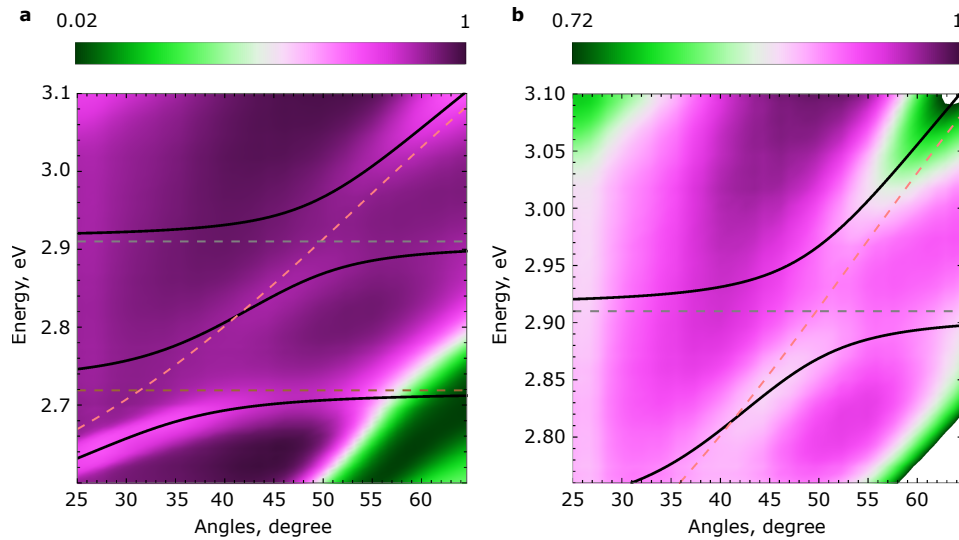


Figure 3.4: Reflectivity map of the optical microcavity obtained by the ellipsometer. (a) The reflectivity map shows the presence of the three polariton branches. (b) Zoomed-in part of the map demonstrates clear anti-crossing between MPB and UPB.

3.3 Experiment

In all experiments on polariton condensation presented in this thesis, one excitation source is employed. High energy Ti:Sapphire regenerative amplifier

(Coherent Libra-HE) produces 100 fs pulses with 800 nm center wavelength at 1 kHz repetition rate. Subsequently, this radiation is used as a pump for the optical parametric amplifier (OPA Coherent OPerA SOLO), which delivers a broad tuning range. The output emission of the OPA is then spectrally filtered with longpass and shortpass edge filters (LP and SP) and is focused at the optical microcavity to a 250 μm spot with a lens with 750 mm focal length. The angle of incidence is adjusted to 45° in order to minimize reflection losses. In the experiments demonstrated in this chapter, the pump center wavelength is tuned in 2.7-2.9 eV range keeping the same full width of half maximum (FWHM) ~ 30 meV. The excitation power is changed by a variable neutral density (ND) filter. To monitor the incident pump density, a calibrated Si photodetector (Thorlabs-Det10/M) and an oscilloscope (Keysight DSOX3054T) are utilized. For the calibration, a Si photodiode (Thorlabs-S120VC) connected to a power meter console (Thorlabs-PM100D) is employed. The output luminescence from the sample is collected by an objective with 0.28 numerical aperture (NA) and coupled to a 750 mm spectrometer (Princeton Instruments SP2750) with a lens with 400 mm focal length. The spectrometer is equipped with an electron multiplying charge-coupled device (EMCCD) camera (Princeton Instruments ProEM 1024BX3) imaging the entrance slit plane. The internal multi grating turret allows for fast switching between the photoluminescence image and the photoluminescence spectrum. For the full excitation/detection optical scheme, see Figure 3.5.

For momentum-space (or k-space) detection an additional 1000 mm k-space lens on a flip mount is added. It projects the Fourier plane of the collecting objective on the entrance slit of the spectrometer. The Fourier plane can be regarded as a map of emission angles. Indeed, all rays emitted by the sample

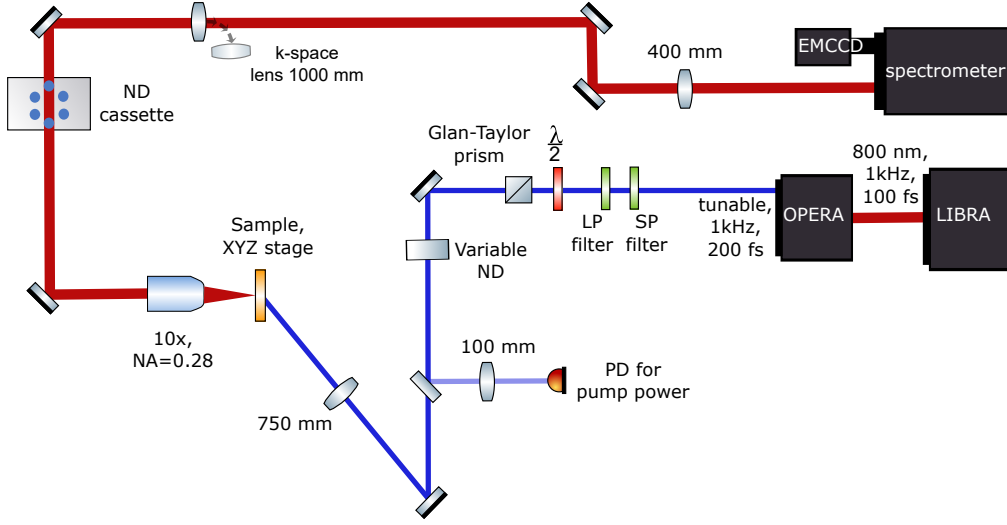


Figure 3.5: Setup for the experiment described in Chapter 2. The excitation beam can be accurately tuned. The detection part enables both energy-resolved real space and momentum space imaging.

at a certain angle θ form a point in the Fourier plane. In turn, the emission angles are directly connected with the in-plane momentum of polaritons:

$$k_{\parallel} = n_{eff} \frac{2\pi}{\lambda_c} \tan\left(\sin^{-1}\left(\frac{\sin(\theta)}{n_{eff}}\right)\right) \approx \frac{2\pi}{\lambda_c} \theta \quad (3.1)$$

where λ_c is the wavelength of the polariton mode. The last approximation is valid for small angles of emission defined by the collecting objective NA (0.28 gives $\theta \in (-16.28^\circ; +16.28^\circ)$). Along the vertical direction (y-axis) a slice of the Fourier plane image is cut by the slit (Figure 3.6a) and subsequently is spectrally resolved along the horizontal x-axis. At the end of the day, such an experimental configuration allows for direct visualization of the polariton energy versus in-plane momentum (e.g. polariton dispersion). The result dispersion is presented in Figure 3.6b.

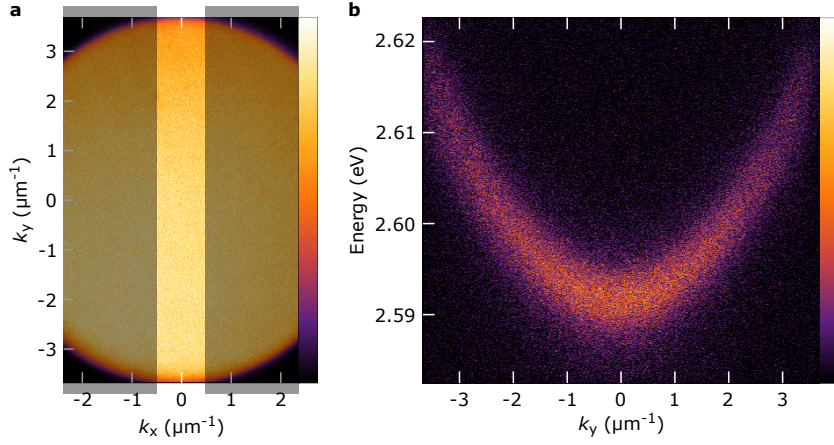


Figure 3.6: Momentum-resolved spectroscopy. (a) The Fourier plane projection on the spectrometer slit (depicted as gray transparent rectangles) results in k -space imaging of polariton luminescence. The slit cut the image along y -axis (b) The result polariton dispersion obtained by dispersing the energy of the Fourier plane slice.

3.4 Results and discussion

Following the idea of "quasi-resonant" excitation stated in the introduction, we choose the strongest vibronic resonance (~ 200 meV) to provide expected vibron-mediated relaxation of pumped excitons towards the ground polariton state. Accordingly, we tune the pump photon energy to 2.8 eV being 200 meV greater than the ground polariton state energy (2.6 eV). Figure 3.7 represents the full energy structure of the organic microcavity and relevant relaxation paths. As was discussed in Chapter 2 and Section 3.2, upon "quasi-resonant" excitation "hot excitons", e.g. excitons dressed with vibrational energy, are formed (the red area). Hot exciton reservoir predominantly relaxes within 100 fs towards $S_{1,0}$ state (the blue area) by means of IC (the blue arrow). One can consider the IC process as losses for the polariton ground state

population, which should be sufficient to achieve polariton condensation. Therefore, vibron-mediated relaxation (the black arrow) should be efficient enough to compete with IC.

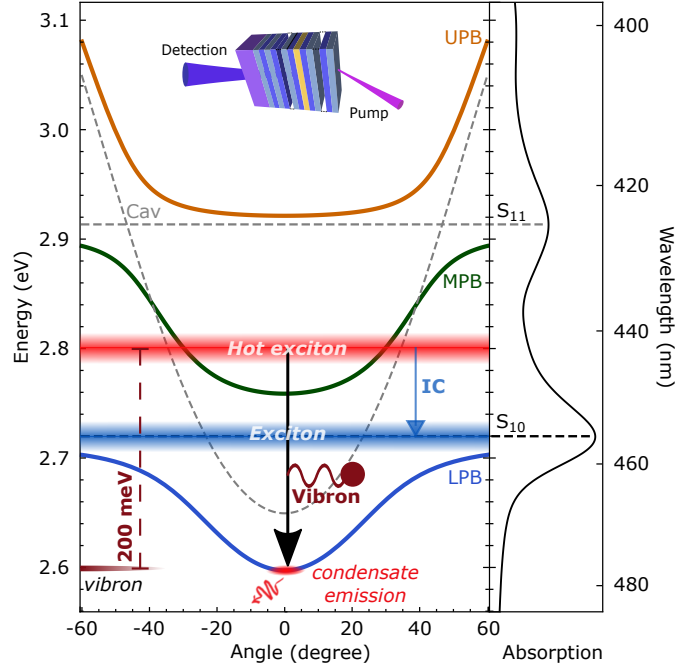


Figure 3.7: The organic microcavity energetic structure and relevant relaxation paths upon "quasi-resonant excitation". Injected hot exciton reservoir (the red area) has two competing relaxation ways: 1) fast (within 100 fs) relaxation towards $S_{1,0}$ level (the blue area); 2) one-step relaxation forming polariton population in the ground state accompanied with the vibron emission (200 meV).

Varying the excitation power, output polariton emission is studied. After a critical incident excitation density $\sim 82 \mu\text{J cm}^{-2}$, a substantial nonlinear increase of the emission intensity is observed. Figure 3.8a shows time-integrated normalized lower polariton branch dispersion above the threshold clearly indicating the energy blueshift (the white dashed line is a fit for

LPB below the threshold). Emission integrated in the vicinity of $k_{\parallel} = 0$ (over $\pm 0.5 \mu\text{m}^{-1}$) versus pump excitation density is plotted in Figure 3.8b. The observed blueshift is accompanied with a sudden decrease of spectral linewidth after the threshold. The spectral characteristics behaviour (Figure 3.8c) and the nonlinear increase of the emission intensity are interpreted as polariton condensation formed in the ground state.

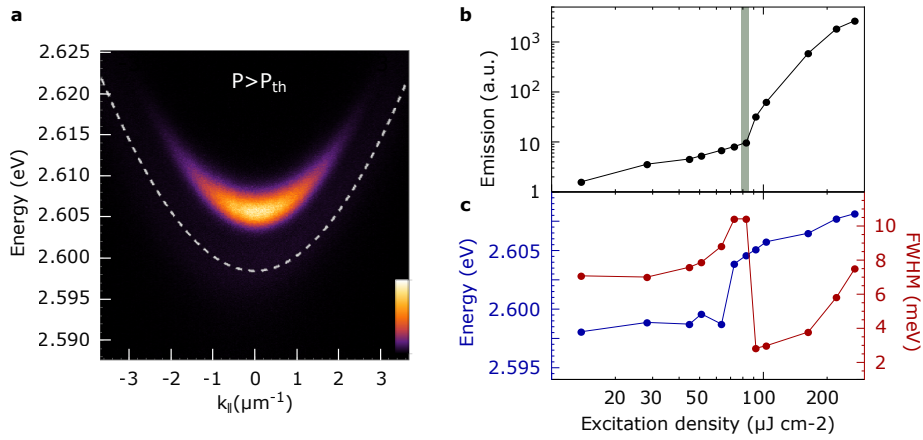


Figure 3.8: Polariton condensation upon "quasi-resonant excitation". (a) Normalized output emission image of the LPB dispersion above the threshold. The white dashed line is a fit for LPB below the threshold. (b) Output emission integrated over $k_{\parallel} = 0 \pm 0.5 \mu\text{m}^{-1}$ versus excitation density. The gray shaded area indicates the threshold. (c) Spectral characteristics (peak position of the emission spectrum - right/blue axis and the full width of half maximum (FWHM) - left/red axis) versus excitation density.

In order to get more insight into the vibron-mediated relaxation efficiency, we perform additional experiments. A wedged structure of the cavity provides accurate control over the cavity length. Consequently, a broad range of exciton-photon detuning and corresponding ground polariton state energy can be accessed. Varying the investigated place on the sample, we explore

how polariton emission intensity correlates with the ground polariton state energy. In contrast to the previous experiments, we fix the pump photon energy at 2.72 eV in resonance with $S_{1,0}$ state in order to minimize IC effects. Figure 3.9 shows output emission intensity dependence on the ground polariton state energy (bottom x-axis). The top x-axis presents corresponding energy difference between the ground state and the excitation photon. We observe that the peaks of the dependence perfectly match Raman spectrum resonances V1 and V2 (the top graph). The observed correlation clearly shows that under resonant conditions ($\hbar\omega_{exciton} = \hbar\omega_{vibron} + \hbar\omega_{polariton}$) efficient relaxation towards the ground state occurs.

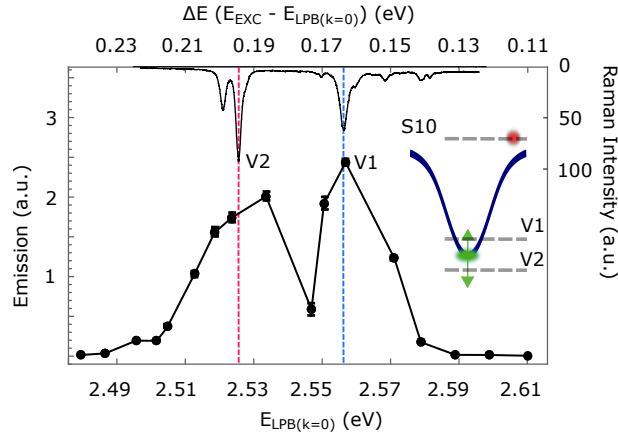


Figure 3.9: Output emission intensity versus the ground polariton state energy with fixed pump photon energy. The top x-axis presents corresponding energy difference between the ground state and the excitation photon (2.72 eV). The top graph depicts the Raman spectrum of MelPPP. The peaks of the measured dependence perfectly correlate with the vibronic resonances V1 and V2, e.g. when $\hbar\omega_{exciton} = \hbar\omega_{vibron} + \hbar\omega_{polariton}$

To further support this experimental evidence, we fix the ground polariton

state energy at 2.6 eV and monitor the output emission under hot excitons injection. Varying the pump photon energy, a steep rise near 2.8 eV is observed (Figure 3.10, the emission is plotted in logarithmic scale). Notably, pumping at 2.8 eV produces almost two orders of magnitude higher emission intensity than the excitation resonant with the absorption maximum (2.72 eV). The experiment clearly indicates the profound role of vibron-mediated relaxation of the hot exciton reservoir.

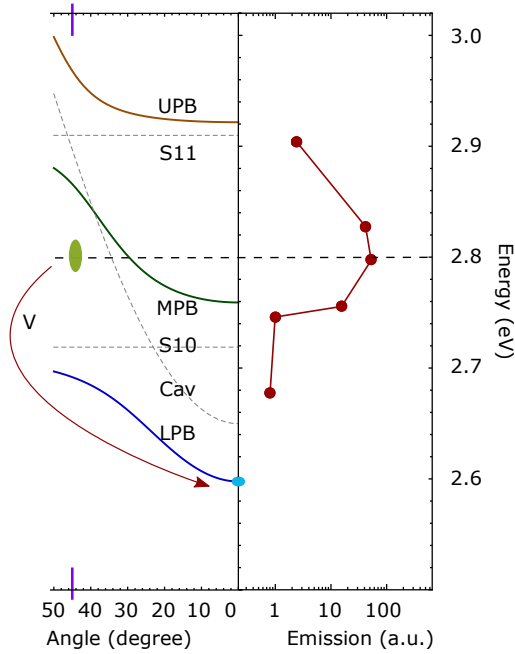


Figure 3.10: Output emission intensity versus the excitation photon energy with fixed ground polariton state energy. The dependence is plotted together with the polariton branches (left panel). The optical pump injects hot exciton reservoir. An increase of the emission intensity is observed when the resonant condition $\hbar\omega_{exciton} = \hbar\omega_{vibron} + \hbar\omega_{polariton}$ is met.

In this chapter, polariton condensation upon "quasi-resonant" excitation is

achieved. While previous experimental works explored the important role of molecular vibrations in polariton states population below the condensation threshold, for the first time we observe similar correlations in the condensation regime. By thorough experiments, we show the presence of one-step hot exciton reservoir relaxation, which mediates the formation of polariton condensation. This relaxation mechanism turns out to be quite efficient to compete with molecular internal conversion processes depopulating the hot exciton reservoir. Notably, the observed condensation threshold value ($\sim 82 \mu\text{J cm}^{-2}$) is almost one order of magnitude smaller than the one demonstrated under non-resonant excitation at 3.1 eV [29] in the same structure, while the MelPPP absorption is only twice larger at 2.8 eV than at 3.1 eV. We reexamine this result and obtain almost the same threshold value as in [29] $\sim 1000 \mu\text{J cm}^{-2}$. Our findings provide a useful receipt for experiments aiming to achieve polariton condensation in strongly-coupled organic microcavities.

3.5 Intracavity nonlinear refractive index influence

The polariton energy-shift at condensation was observed in several organic microcavities [29–31,57]. This phenomenon is considered to be a consequence of polariton interactions in inorganic structures [68,69]. However, the organic blueshift cannot be explained in the same way due to the localized nature of organic excitons that weakens interparticle interactions. Potentially, one can suggest that the mode energy shifts due to a change of nonlinear refractive index of an organic medium induced by the dramatic increase of the intracavity electric field at the condensation threshold. Based on the polariton condensation in a BODIPY-G1-filled microcavity, we explore how the nonlin-

ear refractive index of the intracavity material affects the polariton blueshift. In [70], the colleagues performed single-shot experiments on the polariton condensation in BODIPY-G1 microcavities. Further research revealed the mode blueshift up to 5 meV in a broad range of exciton-photon detuning [Reference 3 of the list of publications]. To estimate the field intensity inside the cavity, we record a real-space image of the condensate ($P_{pump} = 1.4P_{th}$) on the EMCCD camera. Initially, we calibrate the camera with a 140 fs laser pulse with the center wavelength 550 nm (approximately coincides with the polariton condensation wavelength) and known pulse energy. In this way, we calculate the condensate emission intensity:

$$I_0 = \frac{2W_c}{\tau\pi r^2} \quad (3.2)$$

where $W_c=0.5$ pJ is the condensate pulse energy, $\tau=100$ fs - polariton lifetime and r - radius of the real space image profile. Since the intracavity field is considered as a standing wave damped oscillations, then for the field inside the cavity:

$$E_c(t, x) = E_c(x) \exp\left(\frac{-\omega_c t}{Q}\right) \exp(-i\omega_c t) \quad (3.3)$$

where ω_c is the cavity eigenfrequency, Q is a quality factor and E_c presents the field distribution. Obviously, the maximum intensity is reached at $t=0$ in the standing wave antinode $I_c = |E_c(0, \frac{L_c}{2})|^2$, where L_c is the length of the cavity. Considering the simplest case of a symmetric cavity with DBRs reflectance R , we find the relation between intensities for the intracavity field maximum and the outgoing emission I_0 :

$$I_0 \approx (1 - R) \frac{I_c}{4} \quad (3.4)$$

Here we take into account that the standing wave is the result of two equivalent counter-propagating waves interference. As long as Q is estimated at ~ 350 , I_c is equal to 2.2 GW/cm^2 . To measure the refractive index change contribution, we examine nonlinear optical properties of a bare intracavity film by a well-known Z-scan technique [71]. The experimental configuration and automation in LabView is realized by the author and utilized to explore optical properties of hexadecachloro-substituted lanthanide (III) phthalocyaninates in conjugation with gold nanoparticles in [Reference 2 of the author's list of publications]. Figure 3.11 depicts the setup. Coherent Opera Solo produces 140 fs pulses with 545 nm central wavelength and 10 Hz repetition rate. Then, the beam is focused in $16 \mu\text{m}$ spot radius by a lens with 100 mm focal length. While a Si photodetector PD1 (Thorlabs-Det10/M) is used as a reference, PD2 and PD3 record open and closed aperture data, respectively. The aperture is adjusted for 50 % of transmission. The photodetectors are connected with an oscilloscope (Keysight DSOX3054T). The sample is moved across the z-axis by a motorized translation stage (Thorlabs TravelMax 50 mm connected to Thorlabs 50 mm Trapezoidal Stepper Motor Drive). The open-aperture measurements (ratio PD2/PD1 versus the z position of the sample) can result in a peak or a valley at the beam focus position (e.g. $z=0$). This behavior is explained by nonlinear absorption, which reaches its maximum at the beam waist.

The closed-aperture measurements are used for nonlinear refraction index calculation and is usually plotted as $\frac{(PD3/PD1)}{(PD2/PD1)}$ versus the z position of the sample. The denominator is normalization for excluding the nonlinear absorption influence. Generally, the dependence looks like a symmetrical curve with a peak and a valley on both sides of the focus due to self-focusing or de-focusing effects, which result in position-dependent transmission through

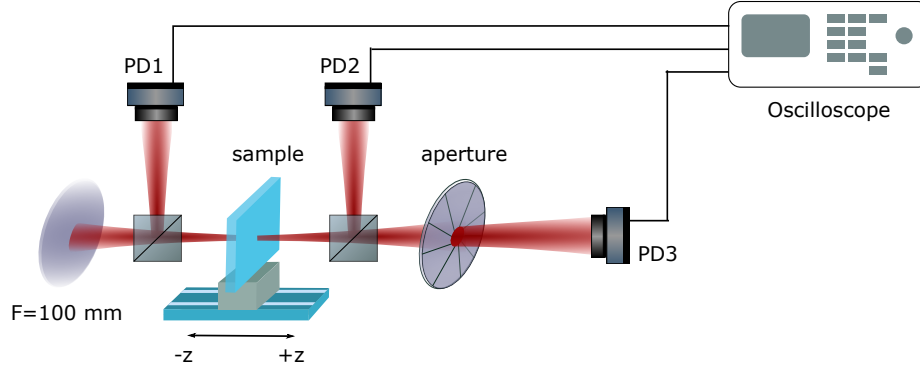


Figure 3.11: Schematic of Z-scan setup.

the aperture.

We study two films: BODIPY-G1 in a polystyrene host matrix and pure polystyrene with 600 nm thickness. We don't observe any nonlinear change of absorption and refraction for both films under illumination with intensity 17 GW/cm^2 , one order of magnitude more than the estimated intracavity intensity (Figures 3.12a and 3.12b, violet circles). At higher incident intensity 779 GW/cm^2 we find, that pure polystyrene film exhibits self-focusing effect and positive nonlinear absorption (Figures 3.12a and 3.12b, blue diamonds). We fit the data with analytical curves and extract nonlinear refractive index ($n_2=1.89 \times 10^{-14} \text{ cm}^2/\text{W}$) and nonlinear absorption coefficient ($\beta=3.42 \times 10^9 \text{ cm/W}$). We note that the BODIPY-G1 film doesn't show nonlinear effects up to 779 GW/cm^2 where it undergoes photobleaching. We conclude that nonlinear refractive index change is not responsible for the polariton energy shift.

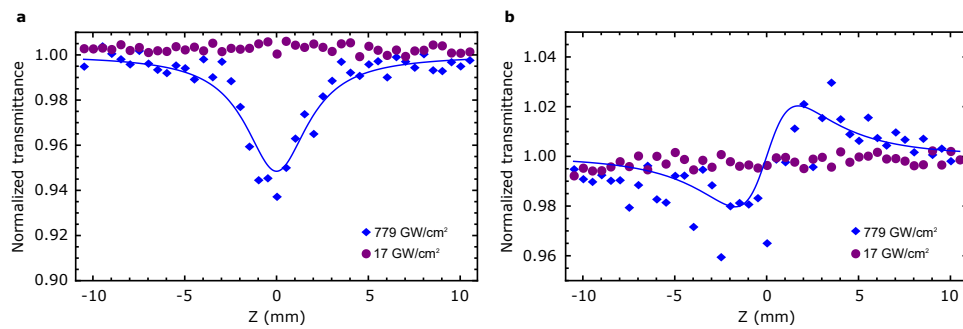


Figure 3.12: Z-scan results for the pure polystyrene film. (a) Open-aperture data for low (violet circles) and high (blue diamonds) intensity. (b) Close-aperture data for low (violet circles) and high (blue diamonds) intensity. The solid line depicts fitting curves for both plots.

Summary: In this chapter, we introduced the investigated organic micro-cavity, including the optical properties of the intrinsic medium and coupled oscillator model. Then, we presented the experimental methods for excitation and detection. Finally, we achieved the polariton condensation, demonstrated necessary power dependences, and proved the vibronic relaxation of excitons towards the ground polariton state. Moreover, we explored another organic material system to confirm that the observed blueshift is not caused by the nonlinear refractive index of the intracavity material.

Chapter 4

Polariton amplification

4.1 Introduction

As outlined in Chapter 2, the physics of strong light-matter interaction brings an opportunity to demonstrate optical amplification [21,49]. This effect arises from polariton-polariton interactions in inorganic strongly-coupled microcavities. Such interactions are driven by the excitonic counterpart and therefore, strongly depends on the intracavity material structure and morphology. In organic materials case, localization of Frenkel excitons on separate molecules suppresses their Coulomb interaction. This fact together with typically shorter polariton lifetimes prevent polariton-polariton interactions in organic microcavities [35]. Thanks to this limitation, on-demand polariton condensation similar to [21] still wasn't demonstrated [35]. Consequently, optical amplification in organic microcavities remains elusive.

This chapter demonstrates another approach to the problem based on the interesting physics revealed in Chapter 3. We exploit "quasi-resonant" excitation introduced above. Utilizing the pump-probe technique similar to [21], polariton amplification is demonstrated driven by the final state stimulation

and vibron-mediated relaxation. The observed phenomenon brings optical amplification of a weak probe signal with gain coefficient up to 6500 times or net gain ~ 10 dB μm^{-1} for an equivalent homogeneous medium.

4.2 Experiment

The pump-probe measurements presented in this Chapter are based on the experimental setup discussed in Chapter 3. In addition to the pump beam, the probe beam is introduced as follows (Figure 4.1). The residual 800 nm pump pulse coming out from Coherent OPerA SOLO is focused on a sapphire plate. The produced broadband white light continuum (WLC) is then spectrally filtered in the energy range 2.47-2.8 eV (Figure 4.2a) having the pulse duration 400-600 fs. Finally, the probe beam is focused on the sample by a lens with 150 mm focal length to 600 μm spot size. The angle of incidence is adjusted to 0° . Such a probe beam arrangement enables us to seed the ground polariton state in a quite broad range of exciton-photon detuning. The momentum and energy resolved image of the transmitted probe is depicted in Figure 4.2b, illustrating the seeding. The focusing lens provides rather small input aperture (± 0.5 μm^{-1} or $\pm 2^\circ$). The corresponding transmission spectrum is shown in Figure 4.2c. Evidently, it represents a peak at the ground polariton state energy. Since all the experiments are carried out under pulsed excitation, the pump and probe beam optical paths are corrected to have the same length. A motorized translation stage with a retroreflector is used in the probe beam path to vary the temporal overlap between the pump and probe pulses.

To detect the weakest optical signals, a hybrid photomultiplier tube (HPT) is employed (Becker and Hickl HPM 100-06). The applied voltage and the

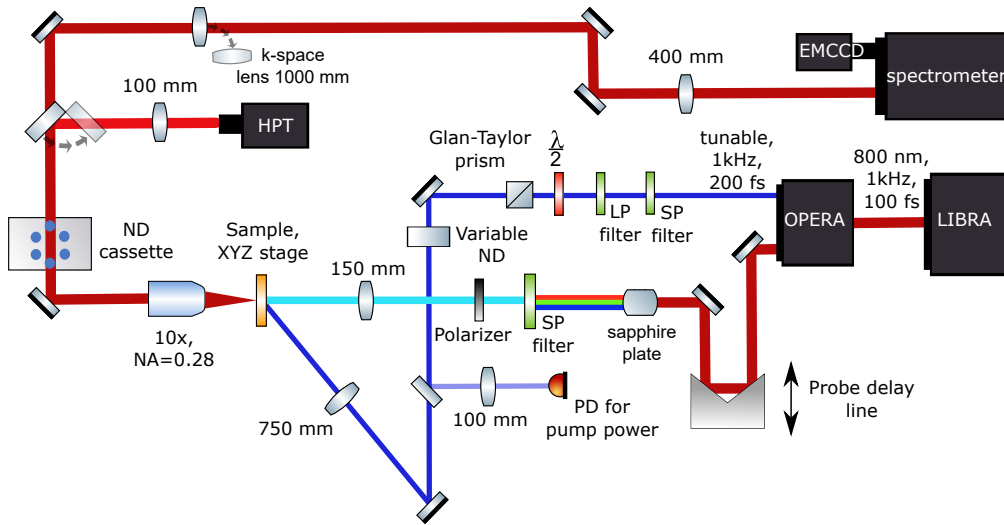


Figure 4.1: Simplified schematic of the pump-probe setup. The detection part enables both energy-resolved real space and momentum space imaging. A flip mirror allows switching between the spectrometer and HPT for the weakest signals detection. The broadband probe beam is produced by WLC generation in a sapphire plate excited by residual 800 nm pump coming out from OPERA. The probe beam hits the sample at normal incidence seeding the ground polariton state.

HPT gain are controlled by the DCC-100 module. In contrast to conventional photomultiplier tubes, the hybrid one has a simplified structure. After light strikes an input photocathode, the emitted photoelectrons are accelerated towards an avalanche photodiode (APD) with a huge gain (typically several 10000 times). Owing to the absence of dynodes and simpler structure, HPT possesses better signal stability and reduced afterpulse effect. To sample the photomultiplier tube output, it is connected with an oscilloscope (Keysight DSOX3054T). The linearity of the detector is tested using a Si photodiode (Thorlabs-S120VC) connected to a power meter console (Thorlabs-PM100D).

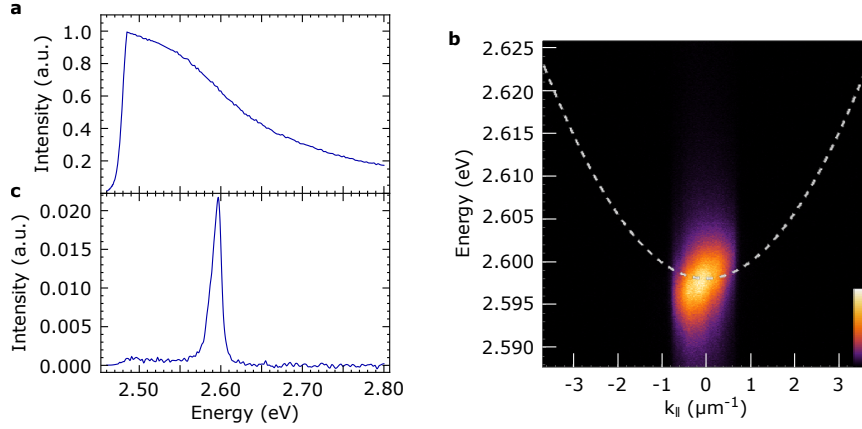


Figure 4.2: Seeding the ground polariton state. (a) The spectrum of the broadband probe before the sample. (b) Energy and momentum resolve emission image obtained with the seeding by the probe. The white dashed line is a fit for LPB below the threshold (c) The spectrum of the probe after the sample.

4.3 Organic polariton amplifier

The presence of another optical beam resonantly seeding the ground polariton state is expected to trigger polariton condensation by means of bosonic stimulation as shown in [21]. In principle, there is no need to work in the nonlinear regime (e.g. above the threshold for the pump excitation density). Indeed, the stimulation rate scales with the occupancy of the final state (the ground polariton state in this case) as $N+1$. The resonant seeding directly creates the final state occupancy, which could exceed the one originated from excitons relaxation in the "pump-only" case below the threshold. As a result, the probe beam accelerates the relaxation towards the ground polariton states leading to the condensate formation. Figure 4.3 presents the impact of preexisting polariton occupancy created by the probe beam. While Figure

4.3a and Figure 4.3b are dispersion images in "probe-only" and "pump-only" cases, Figure 4.3c is produced by the simultaneous presence of the two beams with the same excitation conditions. It can be deduced that even below the condensation threshold, the seeding leads to enhancement of the emission intensity and rigid blueshift.

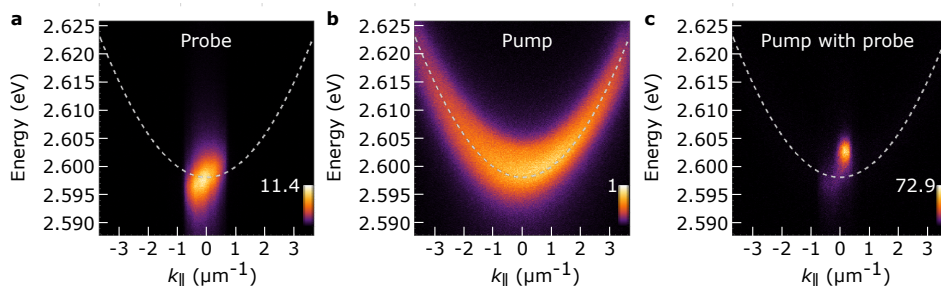


Figure 4.3: The stimulation impact. (a) The dispersion image in the presence of the probe beam only. The white dashed line is a fit for LPB below the threshold. (b) The dispersion image in the presence of the pump beam only. (c) The dispersion image produced by both beams simultaneously hitting the sample. Integrated intensity is much greater than the summation of the "pump-only" and "probe-only" images.

To confirm the usual condensation hallmarks, we explore the same dependencies as for the "pump-only case" in Chapter 3. Figure 4.4a shows the emission integrated near $k_{||} = 0$ (over $\pm 0.5 \mu\text{m}^{-1}$) versus pump excitation density, while Figure 4.4b presents the corresponding peak energy position of the emission spectrum and FWHM. Interestingly, the transition from linear to nonlinear regime occurs at twice lower threshold than in the "pump-only" case ($\sim 49 \mu\text{J cm}^{-2}$ in comparison with $\sim 82 \mu\text{J cm}^{-2}$). We detect spectral signatures inherent to condensation: spectral linewidth narrowing and blueshift. These observations support the assumption of polariton conden-

sation mediated by the probe beam stimulation.

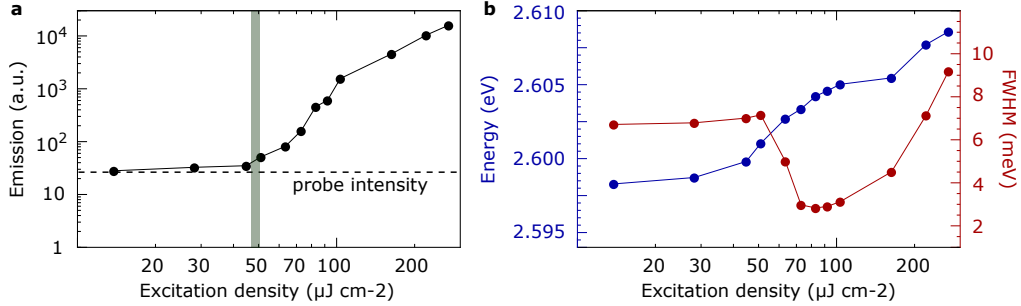


Figure 4.4: Polariton condensation driven by the probe seeding. (a) The emission integrated near $k_{\parallel} = 0$ (over $\pm 0.5 \mu\text{m}^{-1}$) versus pump excitation density. The gray shaded area indicates the threshold. The dashed horizontal line indicates the pure probe intensity. (b) Spectral characteristics (peak position of the emission spectrum - right/blue axis and the full width of half maximum (FWHM) - left/red axis) versus excitation density. The probe beam fluence is kept at $\sim 20 \text{ nJ cm}^{-2}$.

Together with the reduced threshold, "pump-probe" polariton condensation excels in higher relaxation efficiency. Figure 4.5a depicts the output emission intensity as a function of pump excitation density for "pump-only" (blue points) and "pump-probe" (red points) cases. Note that we subtract the pure probe intensity from pump-probe emission for accurate comparison. The integrated emission intensity of "pump-probe" condensation turns out to significantly exceed the "pump-only" condensation intensity. It unambiguously implies enhancement of the relaxation rate towards the ground polariton state owing to bosonic stimulation. We plot the ratio of emission intensity for both cases (Figure 4.5b). Evidently, it has the highest value just before the "pump-only" condensation threshold reaching 50 times and then slightly decreases with excitation power to 5-6 times in the saturation regime.

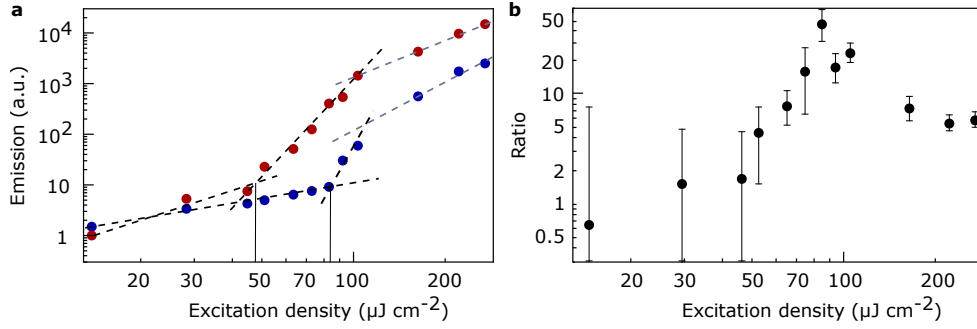


Figure 4.5: Comparison of "pump-probe" polariton condensation with the "pump-only" condensation. (a) The output emission intensity as a function of pump excitation density for "pump-only" (blue points) and "pump-probe" (red points) cases. Dashed lines show fits for linear, nonlinear and saturation regimes. (b) The ratio between both cases calculated from the (a) plot.

Similar to inorganic systems, "pump-probe" polariton condensation brings optical amplification. Figure 4.6a shows the principle of a polariton amplifier. In the absence of the pump beam, a weak transmitted probe signal in the output is observed (Figure 4.6b, black line). However, when the pump beam is on, the signal is dramatically amplified driven by the polariton condensation (Figure 4.6b, blue line).

In order to quantitatively characterize the amplifier we introduce signal amplification coefficient SA as $SA = \frac{P_2 - P_1}{P_0}$, where P_2 and P_0 is power for the transmitted probe signal with and without the pump beam, P_1 is power of the output emission produced by the pump beam itself. To find out the maximum SA , we study the amplification varying the incident probe fluence while pump excitation density is kept constant at $180 \mu\text{J cm}^{-2}$. Such value is chosen to be at the saturation regime and consequently minimize errors caused by the laser power fluctuations and nonlinear response of the sample. We plot the dependence both for SA (Figure 4.7, left/black axis) and a net

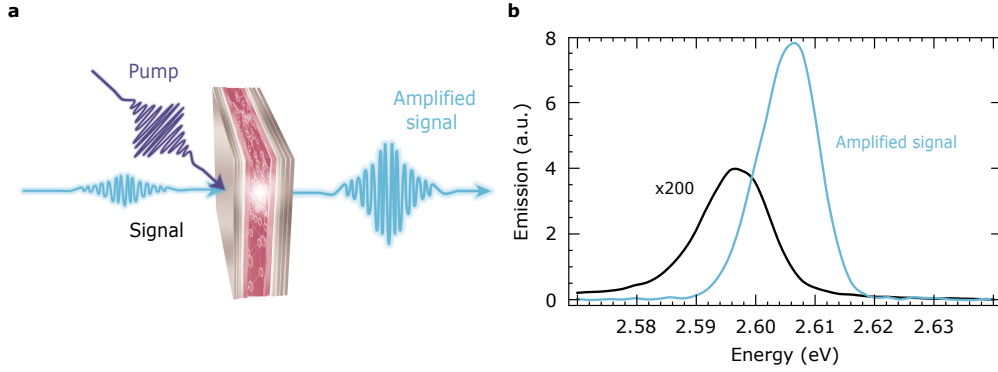


Figure 4.6: Polariton amplifier. (a) Schematic of an amplifier driven by "pump-probe" polariton condensation. (b) Transmission spectrum of the probe beam with (blue line) and without the pump beam (black line). For easier comparison the non-amplified probe is multiplied by 200.

gain in $\text{dB } \mu\text{m}^{-1}$ (Figure 4.7, right/red axis). The net gain of the amplifier represents a gain of equivalent homogeneous medium with given losses. It is written in the following form:

$$g_{net} = 10(\log_{10} SA + \log_{10} \alpha) / L_{eff} \quad (4.1)$$

where α is attenuation coefficient for an input signal, e.g. ($P_0 = \alpha P_{in}^{signal}$, P_{in}^{signal} is power of the input signal), $L_{eff} = 2.35 \mu\text{m}$ is the length of the microcavity structure. In the case of our amplifier, losses are comprised of reflection, absorption, and scattering of the input probe signal. Measuring the ratio between input and transmitted signal in the spectral range of interest (namely the bandwidth of the ground state polariton mode), α is found to be 0.029. In this way, the amplification reaches the maximum value at the lowest probe fluence giving $SA = 6500$ and $g_{net} = 9.7 \text{ dB } \mu\text{m}^{-1}$. The gray shaded area on Figure 4.7 indicates probe fluence values where the difference

between pump and pump-probe signals is masked by fluctuations.

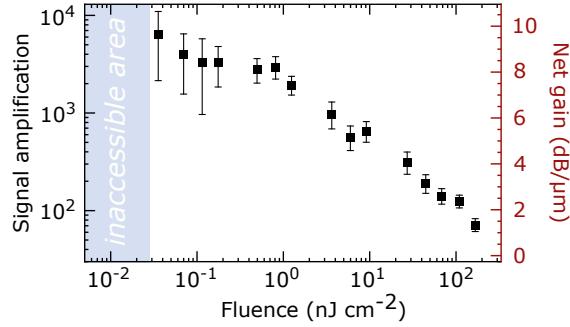


Figure 4.7: Amplification versus incident probe fluence. The amplification is presented as SA (left/black axis) and g_{net} (right/red axis)

Remarkably, the amplifier turns out to operate in both directions: in transmission and reflection configurations with almost the same SA (see Figure 4.8 together with schematics of transmission and reflection configurations). Being a highly reflective structure, the microcavity reflects 66.1% of the input signal in the spectral region of interest. By substituting $\alpha = 0.661$ into (4.1) we obtain $g_{net} = 15.5 \text{ dB } \mu\text{m}^{-1}$.

The demonstrated organic polariton amplifier has several advantages in comparison with the inorganic one. The most striking point is that the result offers the amplifier operation at ambient conditions. Despite, there is no need to adjust the pump angle in order to match the momentum conservation law, the crucial condition for inorganic polariton amplifier. Indeed, the vibronic scattering mechanism is not limited by the momentum conservation law [72]. Nevertheless, we explore the optical amplification under different angles of the pump beam in the saturation regime (Figure 4.9). As expected, the amplification is observed in a broad range of angles. Yet, there is a slight decrease of SA for smaller angles. The reason for this is not well understood and can be related to better overlapping of the pump and probe spots at

higher angles or possible waveguiding modes.

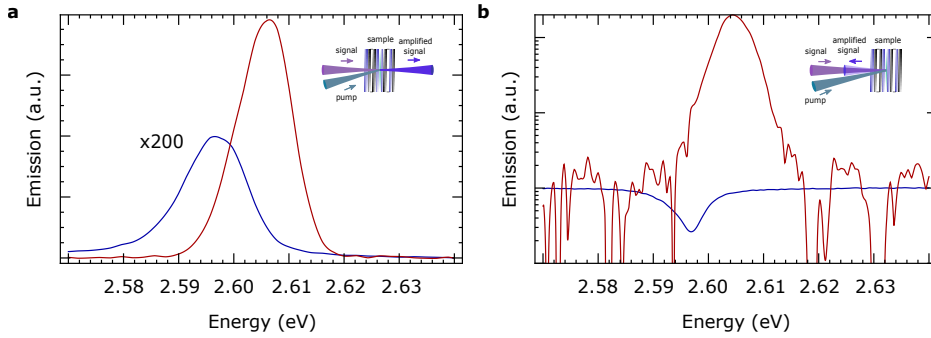


Figure 4.8: Bidirectional amplification. (a) The weak transmitted probe signal (blue line) is amplified when the pump beam is present (red line). The non-amplified signal is multiplied by 200 for easier comparison. (b) The reflected probe beam (blue line) is amplified with almost the same SA (red line).

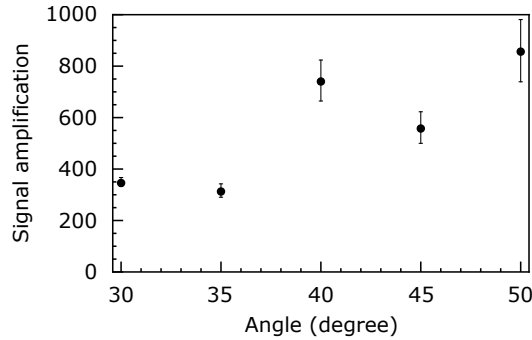


Figure 4.9: Angular dependence of the signal amplification. The probe beam fluence is kept at $\sim 20 \text{ nJ cm}^{-2}$ while the pump power is fixed at $180 \mu\text{J cm}^{-2}$

Regarding the amplification coefficient, our result is a bit better than the best reported for the inorganic polariton amplifier [49] which has near 5000

times with almost twice longer microcavity structure. To complete the discussion on amplification, we expand the comparison to other types of optical amplifiers. Table 4.1 presents the best representatives of other types of optical amplifiers reported to date. To the best of our knowledge, our net gain is found to have a record value. Note that together with the net gain g_{net} we present also $g'_{net} = g_{net}L_{eff}$ expressed in dB, e.g. not normalized by length.

Table 4.1: Amplification coefficients in various types of optical amplifiers. The brackets present values in reflection configuration

Amplifier Type	Ref.	Net gain g'_{net} (dB)	Net gain g_{net} (dB/ μm)	Length (μm)
Organic Polariton Amplifier	This work	22.8 (36.3)	9.7 (15.5)	2.35
VCSOAs	[73]	19	1.94	9.8
QD SOAs	[74]	40	6×10^{-3}	6150
EDWAs	[75]	5.7	0.01	56.2
Plasmonic Amplifier	[76]	11.1	8.5×10^{-3}	1300

Summary: In this chapter, the ultrafast pump-probe technique allowed us to achieve the ground state stimulation by another optical beam. We presented the experimental methods and necessary power dependences to confirm the result polariton amplification. The observed phenomenon brings optical amplification of a weak probe signal with gain coefficient up to 6500 times or net gain $\sim 10 \text{ dB } \mu\text{m}^{-1}$ for an equivalent homogeneous medium.

Chapter 5

All-optical polariton logic

5.1 Introduction

An optical transistor is a fundamental crucial part for all-optical logic circuits. Mainly, it is a switching device able to control light. However, one can be naive about a transistor functionality. To build large all-optical logic architecture, it should satisfy qualitative criteria [9], allowing for proper interconnections. Cascadability (output signal of one transistor should have a right form to feed the other subsequent stage) and fan-out or optical amplification (output signal power of one transistor should be enough to drive at least two subsequent stages) are considered to be the most crucial. In 2013 Ballarini et.al. demonstrated a "proof-of-concept" device satisfying the criteria based on an inorganic strongly-coupled microcavity operating at cryogenic temperature [16]. Moreover, they succeeded in two logic gates realization (AND and OR). Liew et.al. provided a theoretical proposal for all-optical polariton logic circuitry including universal logic [77], however the experimental realization of such structure didn't appear so far. In this chapter, we demonstrate the switching concept and investigate the dynamics of the system. In addition

to already shown amplification, we prove that the developed device possesses cascadability. Utilizing complex double/triple pump-probe techniques, we demonstrate the concept of OR and AND logic gates operation.

5.2 Organic polariton switching

To come up with a principle of transistor switching, the "pump-probe" polariton condensation should be viewed from another perspective. As discussed in Section 4.3, the seeding leads to enhancement of the output emission for the reason of relaxation acceleration (Figure 4.5). Thereby, the output emission intensity with and without the probe beam can be considered as "1" and "0" state, respectively. Figure 5.1a illustrates the switching principle. Hereinafter, we refer to the probe beam and the output signal as control and address due to logic circuits terminology. For a transistor switching operation, "1" and "0" states should be distinguishable. Recalling the results from Section 4.3, the extinction ratio ("1"/"0") is found to reach 50 times or 17 dB in the maximum and slightly decreases with the pump excitation density approaching 5-6 times in the saturation regime (Figure 5.1b). Next, the switching dynamics is examined. Varying the time delay between the optical pulses, we reveal ultrafast switching between "1" and "0" states (~ 500 fs, Figure 5.1c). This value is determined by two factors: the low polariton lifetime (~ 100 fs) and fast dynamics of the hot exciton reservoir.

Turning now to cascadability, a complex double pump-probe setup is built. The pump beam is split by a beamsplitter into Pump 1 and Pump 2. The first stage amplification (Address 1) produced by Pump 1 and the control beam in the point A is retro-reflected to the sample in the point B. Then, the Address 1 is spatially and temporally overlapped with Pump 2, using

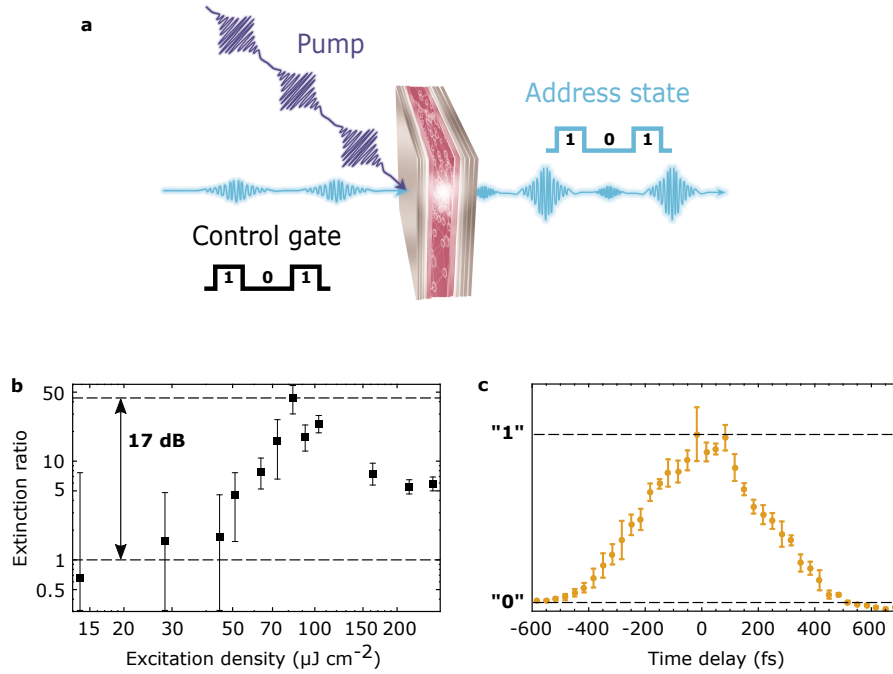


Figure 5.1: Organic polariton switching. (a) The principle of operation. The output emission is regarded as "1" state in the presence of two beams, while the "pump-only" emission is "0" state. (b) Extinction ratio defined as the emission intensity ratio between "1" and "0" states. (c) Output emission intensity of "pump-control" emission versus time delay between the two beams. Ultrafast temporal response of the switching is observed (~ 500 fs at FWHM).

another motorized delay line (Figure 5.2a). In this way, we observe the second stage amplification. Figure 5.2b shows that Address 1 redirected back to the sample induce an undetectable signal in the point B in the absence of Pump 2. When Pump 2 is on, tremendous enhancement of the signal is observed (Figure 5.2c). Evidently, these observations prove the cascability of the amplification.

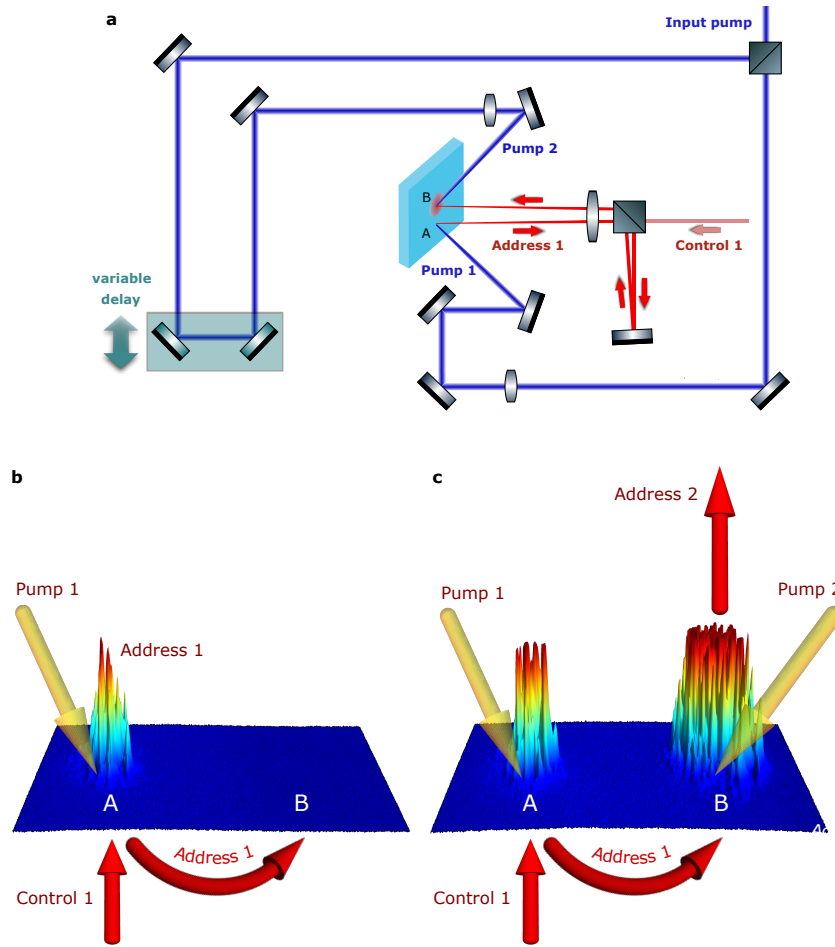


Figure 5.2: Cascadability. (a) Schematic of the double pump-probe setup. (b) First stage amplification in the point A (Address 1, produced by Pump 1 and Control 1) is redirected back to the sample in the point B. The signal in the absence of Pump 2 is undetectable. (c) Pump 2 induces the second stage amplification (Address 2).

5.3 OR and AND polariton logic gates

Here, we employ the same experimental configuration as in the previous section to realize all-optical logic operation principle. Two address states I and II are produced by the overlap of the two control beams with the one

pump: Pump 1. Then, they are retro-reflected to the sample and focused in the same point III, where Pump 2 induces second stage amplification (see schematic in Figure 5.3a). While I and II are regarded as inputs, III is considered as an output of a logic gate. In this way, an AND and an OR gate (see truth tables in Figure 5.3a) can be constructed. The realization of the two gates in the same experimental configuration is only able thanks to two different regimes of the Pump 2 excitation. Namely, Figure 5.3b shows two control power dependences of the output emission for "pump-probe" condensation measured just in one point of the sample. The red dots present the dependence for pump excitation density fixed at $P \sim 2P_{th}$, while the open blue squares - for $P \sim 0.75P_{th}$, where P_{th} is the threshold power for "pump-only" condensation. Clear threshold dependences are observed. One can highlight two peculiarities: pumping in the saturation regime has lower control power threshold (30 pW versus 3 nW) and steeper dependence.

Going back to the gates realization (Figure 5.3a), one can notice that the signal from the point III without Pump 2 is just a linear superposition of the two retro-reflected address beams I and II kept at the same power. Let's consider the amplification in the point III in the presence of Pump 2 upon two excitation regimes described above. The saturation regime of Pump 2 ($P \sim 2P_{th}$) provides no much output intensity difference between amplification for one input and both added together (e.g. following the red curve of Figure 5.3b, the output emission intensities for $P_{control} = 2$ nW and $P_{control} = 2*2$ nW differ by a factor of 1.5). Thus, the truth table for OR gate can be realized. The four panels of Figure 5.3c depicts normalized real space emission images for all input configurations. Conversely, keeping Pump 2 below the threshold, the AND gate can be demonstrated. Indeed, the output emission intensities for $P_{control} = 10$ nW and $P_{control} = 2*10$ nW differ by a factor

of 4-5. Thus, proper adjustment of input powers results in much higher output signal only when both inputs are active. The four panels of Figure 5.3d depict normalized real space emission images for all input configurations demonstrating the AND gate. In this experiment, Pump 2 is kept constant at $P \sim 0.9P_{th}$. We note that in order to overcome pulse-to-pulse fluctuations, the data is obtained in the single-shot regime.

Summary: In this chapter, we exploit the polariton amplification to show the switching concept and verify its fast dynamics. Utilizing sophisticated double pump-probe technique, we proved the cascability of the amplification. In addition, we demonstrate the concept of OR and AND optical gates.

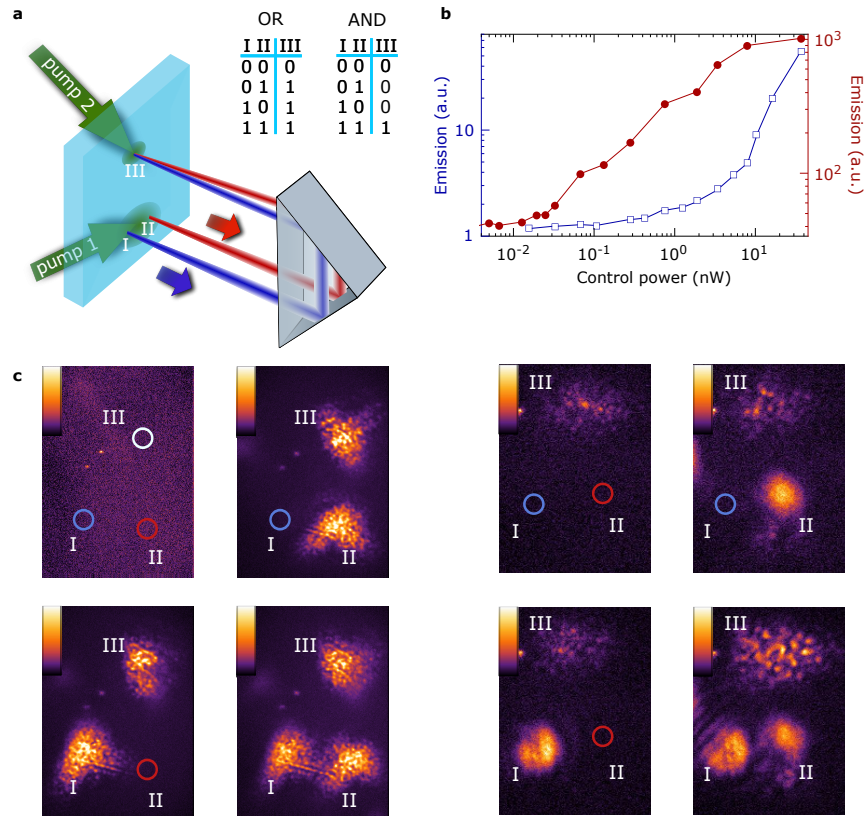


Figure 5.3: All-optical logic gates operation. (a) Schematic of the experimental configuration. Two address states I and II are produced powered by the same pump (Pump 1). Then, they are simultaneously retro-reflected to the point III and amplified by the Pump 2. I, II and III are regarded as two inputs and an output of a logic gate, respectively. The truth tables for an OR and an AND gates are also presented. (b) Control power dependences of the output emission under two regimes of excitation: the saturation regime (red dots) and below the "pump-only" condensation threshold. (c) Normalized real space emission images for all inputs configuration of the truth table for OR gate. (d) Normalized real space emission images for all inputs configuration of the truth table for AND gate.

Chapter 6

Conclusions and future research

This work started with vibron-mediated polariton condensation in the strongly-coupled microcavity containing the MeLPPP polymer. The essential power dependences were measured, while the vibronic relaxation mechanism was proved experimentally. Exploiting the same principle, on-demand polariton condensation was achieved by the ultrafast pump-probe technique. The system is explored as an optical amplifier, and a large net gain coefficient up to $\sim 10 \text{ dB } \mu\text{m}^{-1}$ was found. Further research allowed to show the switching behavior with extinction ratio up to 17 dB and fast dynamics. Having built complex experimental setups, we tested the potential of the system to demonstrate the concept of all-optical logic. We experimentally realize the organic polariton switching principle and showed OR and AND logic gates functionality.

Here, the author expresses his opinion and personal vision for the future. Our work clearly has limitations. Evidently, polariton devices are far away from industrial applications. The fast dynamics of the system gives only the potential to realize THz optical switching. Thanks to the necessity of high excitation intensities in organic microcavities, low repetition rate pulsed

lasers are usually employed, restricting the real speed of the switching. To reduce the polariton lasing threshold, high-quality samples are needed. Ideally, they should possess large Q-factors, a small number of defects and reduced exciton-exciton annihilation effects [78]. Moreover, some technical efforts to decrease the number of uncoupled molecules should be made. Another point could be the improvement of the relaxation efficiency towards the ground polariton state. Indeed, superposing the luminescence peak of the organic material and the polariton mode, one can achieve an additional relaxation path through radiative pumping.

Speaking of the potential small sizes of polariton devices, further research should aim to show logic gates principle on a chip (i.e., without the necessity to use external optical elements). Obviously, cavities with larger propagation length are needed to enable polariton movement from transistor to transistor, similar to [16]. Furthermore, the system should be explored under electrical excitation, which is a challenge for organic devices. A possible solution was proposed by Paschos et.al. [79] as a hybrid organic-inorganic polariton laser. In this work, the researchers combined the electrical injection due to the high carrier mobility of GaAs and high-temperature polariton lasing from J-aggregates. Finishing the discussion of miniaturization, one can argue that the spot sizes on the sample are restricted by the diffraction limit anyway. However, modern nano-optics research revealed the possibility to process light beams beyond this limit [80].

Besides the listed drawbacks, the author believes that this work could be one of the tiny steps towards novel optical devices based on strong light-matter interaction.

Bibliography

- [1] Menzel, R. *Photonics: linear and nonlinear interactions of laser light and matter* (Springer Science & Business Media, 2013).
- [2] Maiman, T. Stimulated optical radiation in ruby. *Nature* **187**, 493–494 (1960).
- [3] Hall, R. N., Fenner, G. E., Kingsley, J., Soltys, T. & Carlson, R. Coherent light emission from gaas junctions. *Physical Review Letters* **9**, 366 (1962).
- [4] Neamen, D. *Semiconductor physics and devices* (McGraw-Hill: New York, 2003).
- [5] Sorokin, P. P. & Lankard, J. Stimulated emission observed from an organic dye, chloro-aluminum phthalocyanine. *IBM Journal of Research and Development* **10**, 162–163 (1966).
- [6] Schäfer, F. P., Schmidt, W. & Volze, J. Organic dye solution laser. *Applied Physics Letters* **9**, 306–309 (1966).
- [7] Träger, F. *Springer handbook of lasers and optics* (Springer Science & Business Media, 2012).

- [8] Tang, C. W. & VanSlyke, S. A. Organic electroluminescent diodes. *Applied physics letters* **51**, 913–915 (1987).
- [9] Miller, D. A. Are optical transistors the logical next step? *Nature Photonics* **4**, 3 (2010).
- [10] Gibbs, H. *et al.* *Controlling light with light: Optical bistability and optical modulation* (Springer, 1979).
- [11] Hwang, J. *et al.* A single-molecule optical transistor. *Nature* **460**, 76 (2009).
- [12] Fushman, I. *et al.* Controlled phase shifts with a single quantum dot. *Science* **320**, 769–772 (2008).
- [13] Mabuchi, H. Cavity-qed models of switches for attojoule-scale nanophotonic logic. *Physical Review A* **80**, 045802 (2009).
- [14] Gao, T. *et al.* Polariton condensate transistor switch. *Physical Review B* **85**, 235102 (2012).
- [15] Liew, T., Kavokin, A. & Shelykh, I. Optical circuits based on polariton neurons in semiconductor microcavities. *Physical Review Letters* **101**, 016402 (2008).
- [16] Ballarini, D. *et al.* All-optical polariton transistor. *Nature communications* **4**, 1778 (2013).
- [17] Weisbuch, C., Nishioka, M., Ishikawa, A. & Arakawa, Y. Observation of the coupled exciton-photon mode splitting in a semiconductor quantum microcavity. *Physical Review Letters* **69**, 3314 (1992).

- [18] Imamog, A., Ram, R., Pau, S., Yamamoto, Y. *et al.* Nonequilibrium condensates and lasers without inversion: Exciton-polariton lasers. *Physical Review A* **53**, 4250 (1996).
- [19] Kasprzak, J. *et al.* Bose–einstein condensation of exciton polaritons. *Nature* **443**, 409 (2006).
- [20] Byrnes, T., Kim, N. Y. & Yamamoto, Y. Exciton–polariton condensates. *Nature Physics* **10**, 803 (2014).
- [21] Savvidis, P. *et al.* Angle-resonant stimulated polariton amplifier. *Physical review letters* **84**, 1547 (2000).
- [22] Lu, T.-C. *et al.* Room temperature polariton lasing vs. photon lasing in a zno-based hybrid microcavity. *Optics express* **20**, 5530–5537 (2012).
- [23] Christmann, G., Butté, R., Feltin, E., Carlin, J.-F. & Grandjean, N. Room temperature polariton lasing in a gan/ algan multiple quantum well microcavity. *Applied Physics Letters* **93**, 051102 (2008).
- [24] Lidzey, D. G. *et al.* Strong exciton–photon coupling in an organic semiconductor microcavity. *Nature* **395**, 53 (1998).
- [25] Lidzey, D. *et al.* Room temperature polariton emission from strongly coupled organic semiconductor microcavities. *Physical review letters* **82**, 3316 (1999).
- [26] Coles, D. M. *et al.* Strong coupling between chlorosomes of photosynthetic bacteria and a confined optical cavity mode. *Nature communications* **5**, 5561 (2014).
- [27] Coles, D. *et al.* A nanophotonic structure containing living photosynthetic bacteria. *small* **13**, 1701777 (2017).

- [28] Kéna-Cohen, S. & Forrest, S. Room-temperature polariton lasing in an organic single-crystal microcavity. *Nature Photonics* **4**, 371 (2010).
- [29] Plumhof, J. D., Stöferle, T., Mai, L., Scherf, U. & Mahrt, R. F. Room-temperature bose–einstein condensation of cavity exciton–polaritons in a polymer. *Nature materials* **13**, 247 (2014).
- [30] Dietrich, C. P. *et al.* An exciton-polariton laser based on biologically produced fluorescent protein. *Science advances* **2**, e1600666 (2016).
- [31] Cookson, T. *et al.* A yellow polariton condensate in a dye filled microcavity. *Advanced Optical Materials* **5**, 1700203 (2017).
- [32] Svelto, O. & Hanna, D. C. *Principles of lasers*, vol. 4 (Springer, 1998).
- [33] Kavokin, A. V., Baumberg, J. J., Malpuech, G. & Laussy, F. P. *Microcavities*, vol. 21 (Oxford University Press, 2017).
- [34] Lagoudakis, K. *The physics of exciton-polariton condensates* (EPFL Press, 2013).
- [35] Sanvitto, D. & Kéna-Cohen, S. The road towards polaritonic devices. *Nature Materials* **15**, 1061–1073 (2016).
- [36] Lakowicz, J. R. *Principles of fluorescence spectroscopy* (Springer Science & Business Media, 2013).
- [37] Pope, M. & Swenberg, C. E. *Electronic processes in organic crystals and polymers* (Oxford University Press, New York, 1999).
- [38] Sauer, M., Hofkens, J. & Enderlein, J. *Handbook of fluorescence spectroscopy and imaging: from ensemble to single molecules* (John Wiley & Sons, 2010).

- [39] Novotny, L. Strong coupling, energy splitting, and level crossings: A classical perspective. *American Journal of Physics* **78**, 1199–1202 (2010).
- [40] Gerry, C., Knight, P. & Knight, P. L. *Introductory quantum optics* (Cambridge university press, 2005).
- [41] Fox, M. *Quantum optics: an introduction*, vol. 15 (OUP Oxford, 2006).
- [42] Deveaud, B. *Physics of Semiconductor Microcavities: From Fundamentals to Nanoscale Devices* (John Wiley & Sons, 2007).
- [43] Dang, L. S., Heger, D., André, R., Boeuf, F. & Romestain, R. Stimulation of polariton photoluminescence in semiconductor microcavity. *Physical Review Letters* **81**, 3920 (1998).
- [44] Laussy, F. P., Malpuech, G. & Kavokin, A. Spontaneous coherence buildup in a polariton laser. *physica status solidi (c)* **1**, 1339–1350 (2004).
- [45] Tartakovskii, A. *et al.* Relaxation bottleneck and its suppression in semiconductor microcavities. *Physical Review B* **62**, R2283 (2000).
- [46] Skolnick, M., Tartakovskii, A. I., Butté, R., Whittaker, D. & Stevenson, R. M. High-occupancy effects and stimulation phenomena in semiconductor microcavities. *IEEE Journal of selected topics in quantum electronics* **8**, 1060–1071 (2002).
- [47] Butté, R. *et al.* Transition from strong to weak coupling and the onset of lasing in semiconductor microcavities. *Physical Review B* **65**, 205310 (2002).

- [48] Stevenson, R. *et al.* Continuous wave observation of massive polariton redistribution by stimulated scattering in semiconductor microcavities. *Physical Review Letters* **85**, 3680 (2000).
- [49] Saba, M. *et al.* High-temperature ultrafast polariton parametric amplification in semiconductor microcavities. *Nature* **414**, 731–735 (2001).
- [50] Michetti, P. & La Rocca, G. C. Exciton-phonon scattering and photoexcitation dynamics in j-aggregate microcavities. *Physical Review B* **79**, 035325 (2009).
- [51] Litinskaya, M., Reineker, P. & Agranovich, V. Fast polariton relaxation in strongly coupled organic microcavities. *Journal of luminescence* **110**, 364–372 (2004).
- [52] Mazza, L., Kéna-Cohen, S., Michetti, P. & La Rocca, G. C. Microscopic theory of polariton lasing via vibronically assisted scattering. *Physical Review B* **88**, 075321 (2013).
- [53] Agranovich, V., Litinskaia, M. & Lidzey, D. G. Cavity polaritons in microcavities containing disordered organic semiconductors. *Physical Review B* **67**, 085311 (2003).
- [54] Michetti, P. & La Rocca, G. Polariton states in disordered organic microcavities. *Physical Review B* **71**, 115320 (2005).
- [55] Ciuti, C., Savona, V., Piermarocchi, C., Quattropani, A. & Schwendimann, P. Role of the exchange of carriers in elastic exciton-exciton scattering in quantum wells. *Physical Review B* **58**, 7926 (1998).
- [56] Yagafarov, T. *et al.* On the origin of blueshifts in organic polariton condensates. *arXiv preprint arXiv:1905.02573* (2019).

- [57] Daskalakis, K., Maier, S., Murray, R. & Kéna-Cohen, S. Nonlinear interactions in an organic polariton condensate. *Nature Materials* **13**, 271 (2014).
- [58] Snoke, D. W. & Keeling, J. The new era of polariton condensates. *Physics Today* **70**, 54–60 (2017).
- [59] Somaschi, N. *et al.* Ultrafast polariton population build-up mediated by molecular phonons in organic microcavities. *Applied Physics Letters* **99**, 209 (2011).
- [60] Coles, D. M., Grant, R. T., Lidzey, D. G., Clark, C. & Lagoudakis, P. G. Imaging the polariton relaxation bottleneck in strongly coupled organic semiconductor microcavities. *Physical Review B* **88**, 121303 (2013).
- [61] Scherf, U., Bohnen, A. & Müllen, K. Polyarylenes and poly (arylenevinylene)s, 9 the oxidized states of a (1, 4-phenylene) ladder polymer. *Die Makromolekulare Chemie* **193**, 1127–1133 (1992).
- [62] Cerullo, G. *et al.* Excited-state dynamics of poly (para-phenylene)-type ladder polymers at high photoexcitation density. *Physical Review B* **57**, 12806 (1998).
- [63] Müller, J., Anni, M., Scherf, U., Lupton, J. & Feldmann, J. Vibrational fluorescence spectroscopy of single conjugated polymer molecules. *Physical Review B* **70**, 035205 (2004).
- [64] Gadermaier, C. *et al.* Dynamics of higher photoexcited states in m-lppp probed with sub-20 fs time resolution. *Chemical physics letters* **384**, 251–255 (2004).

- [65] Baessler, H. & Schweitzer, B. Site-selective fluorescence spectroscopy of conjugated polymers and oligomers. *Accounts of Chemical Research* **32**, 173–182 (1999).
- [66] Cuff, L., Kertesz, M., Scherf, U. & Müllen, K. Interpretation of the vibrational spectra of planarized poly-p-phenylene. *Synthetic Metals* **69**, 683–684 (1995).
- [67] Tian, B., Zerbi, G., Schenk, R. & Müllen, K. Optical spectra and structure of oligomeric models of polyparaphenylenevinylene. *The Journal of Chemical Physics* **95**, 3191–3197 (1991).
- [68] Vladimirova, M. *et al.* Polariton-polariton interaction constants in microcavities. *Physical Review B* **82**, 075301 (2010).
- [69] Sun, Y. *et al.* Direct measurement of polariton-polariton interaction strength. *Nature Physics* **13**, 870 (2017).
- [70] Sannikov, D. *et al.* Room temperature broadband polariton lasing from a dye-filled microcavity. *Advanced Optical Materials* 1900163 (2019).
- [71] Sheik-Bahae, M., Said, A. A. & Van Stryland, E. W. High-sensitivity, single-beam n^2 measurements. *Optics letters* **14**, 955–957 (1989).
- [72] Michetti, P. & La Rocca, G. Polariton-polariton scattering in organic microcavities at high excitation densities. *Physical Review B* **82**, 115327 (2010).
- [73] Laurand, N. *et al.* Performance comparison of gainnas vertical-cavity semiconductor optical amplifiers. *IEEE Journal of Quantum Electronics* **41**, 642–649 (2005).

- [74] Akiyama, T., Sugawara, M. & Arakawa, Y. Quantum-dot semiconductor optical amplifiers. *Proceedings of the IEEE* **95**, 1757–1766 (2007).
- [75] Sun, H. *et al.* Giant optical gain in a single-crystal erbium chloride silicate nanowire. *Nature Photonics* (2017).
- [76] De Leon, I. & Berini, P. Amplification of long-range surface plasmons by a dipolar gain medium. *Nature Photonics* **4**, 382–387 (2010).
- [77] Espinosa-Ortega, T. & Liew, T. C. H. Complete architecture of integrated photonic circuits based on and not logic gates of exciton polaritons in semiconductor microcavities. *Physical Review B* **87**, 195305 (2013).
- [78] Akselrod, G. M., Tischler, Y., Young, E. R., Nocera, D. & Bulovic, V. Exciton-exciton annihilation in organic polariton microcavities. *Physical Review B* **82**, 113106 (2010).
- [79] Paschos, G. *et al.* Hybrid organic-inorganic polariton laser. *Scientific reports* **7**, 11377 (2017).
- [80] Gramotnev, D. K. & Bozhevolnyi, S. I. Plasmonics beyond the diffraction limit. *Nature Photonics* **4**, 83 (2010).